Orbitally Shaken Bioreactors - Viscosity effects on flow characteristics

Andrea Ducci[a,*], Weheliye Hashi Weheliye[a]

[a] *Mechanical Engineering Department, University College London, Torrington Place, WC1E 7JE, UK*

Abstract

Phase resolved PIV measurements were carried out to assess the flow dynamics occurring in orbitally shaken bioreactors of cylindrical geometry when working fluids of increasing viscosity are considered. Study of the phase-resolved flow characteristics allowed to built a Re-Fr map, where four quadrants associated to different flow regimes are identified: in-phase toroidal vortex (low Fr, high Re), out-of-phase precessional vortex (high Fr, high Re), in-phase single vortex (low Fr, low Re), out-of-phase counter-rotating toroidal vortex (high Fr, low Re). Turbulence levels are found to be significant only in the top right quadrant (high Fr, low Re) and scaling of the turbulent kinetic energy obtained with fluid of varying viscosity is obtained by employing the ratio of the operating Froude number to the critical Froude number associated to the mean flow transition, Fr/Fr_c. Estimates of the mean flow strain deformation as well as of the flow dissipative scale are provided, while a comparison is made between the flow circulation times obtained for different regimes.

Keywords: Mixing, Orbitally Shaken Bioreactor, viscosity, circulation time, dissipation rate, kinetic energy, fluid mechanics.

1. Introduction

Shaken bioreactors are extensively used in the early stages of bioprocess development, with micrometer plates (24, 48, 96 or 384 wells) being advantageous for processing a large number of experiments in parallel, while shaken flasks (25 ml - 6 l) are the most widely used type of orbitally shaken reactors (ORS) as they offer a cost-efficient system suitable for a wide range of tasks. In recent years large scale shaken bioreactor systems of 500-2000 l in volume have been developed and introduced at the production scale in the effort to reduce scaling problems, and provide a single piece of equipment suitable for different cell culture processes at multiple scales[1,2]. These large systems are implemented in cylindrical containers usually equipped with a pre-sterilised disposable plastic bag. Despite recent progress of shaken bioreactor platforms, with the development of optical sensors and control loops to improve automation in millilitre scale bioreactors, the number of publications which address scaling up/down aspects of shaken bioreactors is very limited[3].

---

[*] Corresponding author: a.ducci@ucl.ac.uk

The majority of the studies available in the literature, that aimed at an engineering characterisation of the flow in shaken bioreactors, has mainly been carried out with fluids of water-like viscosity[4,5,6,7]. This type of fluid is closer to the culture media most commonly used for growth of mammalian and microbial cells. However, caution should be exerted when micro-organisms characterised by a filamentous morphology are considered. In this case the viscosity of the fermentation broth increases with fermentation time due to the formation of biomass[8]. Büchs et al.[9] report that this viscosity increase over fermentation time will promote out-of-phase conditions with a significant reduction of oxygen transfer and mixing intensity, and altered cell metabolism. In a such a case the whole screening process would unintentionally suffer from inadequate substrate supply to the cells, and would fail to identify improved strains and media. From this perspective the study of Büchs et al.[9] investigated the power consumption of Newtonian fluids with dynamic viscosity up to μ=200 Pa s (cf. water, μ=1 mPa s), while the simulations and flow visualisations of Kim and Kizito[10] provided a qualitative analysis of the time averaged velocity flow fields for $1\times10^{-6}\leq \nu \leq 1.6\times10^{-5}$ m^2/s. The latter study highlighted a significant variation of the cylindrical bioreactor flow dynamics when the viscosity was increased. At low viscosity the flow is characterised by a pair of counter-rotating vortices which merge along the axis of the bioreactor in an upward stream. According to the simulations of Kim and Kizito[10] this flow configuration still persists in the time-averaged flow fields obtained for fluids of higher viscosity, but it is relegated to a smaller region closer to the axis of the bioreactor, because a second set of vortices develops at the wall of the cylindrical reactor. This second set of vortices rotates in the opposite direction to that associated to the vortices dominating the flow when low viscous fluids are used.

Similar considerations were made in the early study of Gardner and Tatterson[11] who investigated the mixing and flow dynamics of a shaken container by means of mixing time measurements through a colorimetric technique. Their experiments were carried out for working fluids of increasing viscosity, $\nu = 1 \times 10^{-6} - 5 \times 10^{-3}$ m^{2}s^{-1}, obtained with different dilutions of corn syrup. A schematic of the mixing time visualisation obtained for the two extreme cases (pure water and pure corn syrup) indicated that for the same working volumes these two conditions are characterised by very different flow dynamics with a toroidal vortex being present in the corn syrup for a speed of 300 rmp for both the fluid volumes considered (V_f = 25 and 50 ml), while with water a precessional vortex was exhibited around the vessel axis at a speed of 100 rpm. Gardner and Tatterson[11] provided a mixing number map as a function of the Reynolds number, $Re = Nd_i^2/\nu$, where three different mixing dynamics are identified depending on the flow occurring in the reactor: toroidal vortex mixing, transitional mixing and turbulent splashing. They concluded that the toroidal vortex regime should produce efficient mixing and keep shear stress levels to a minimum.

A detailed and thorough analysis of the flow occurring in an orbitally shaken reactor is provided by the experimental study of Weheliye et al.[12], who carried out PIV measurements in a cylindrical container with water as working fluid. Their study allowed to derive a flow scaling law based on physical considerations, without resorting to the use of power law correlations. The work covered different internal diameters (d_i=7, 10 and 13 cm), filling volumes (V_f= 3-7 cm), orbital diameters (d_o=2-5 cm), and agitation speeds (N=60-130 rpm) and made use of phase-resolved velocity field and free surface inclination measurements. The scaling law was formulated based on the consideration that the free surface orientation is orthogonal to the resultant force obtained from the vectorial sum of the centrifugal force due to the orbital motion and the gravitational one. Two distinct flow dynamics were distinguished inside the bioreactor depending on the combination of orbital Froude number, Fr_{d_o}, non dimensional fluid height, h/d_i and orbital to cylinder diameter ratio, d_o/d_i. At low Froude number the flow is dominated by a toroidal vortex with the free surface motion being in-phase with the orbital movement of the reactor, while at high Froude number the flow dynamics in the reactor are mainly controlled by a precessional vortex, which is out-of-phase with respect to the cylinder orbit. Weheliye et al.[12] concluded that when the non-dimensional fluid height $h/d_i < (d_o/d_i)^{0.5}$, the transitional speed (i.e. critical Froude number, Fr_c) can be derived from the critical wave amplitude, $(\Delta h/h)_c$, using the two Equations 1, while for $h/d_i > (d_o/d_i)^{0.5}$ Equation 2 must be used.

$$\begin{cases} \frac{h}{d_i} = \left(\frac{h}{\Delta h}\right)_c Fr_{d_o}\, a_{ow} \\ \\ \left(\frac{\Delta h}{h}\right)_c = \left(\frac{d_o}{d_i}\right)^{0.5} \end{cases} \tag{1}$$

$$a_{ow} Fr_{d_i} = 1 \tag{2}$$

where Fr_{d_o} and Fr_{d_i} are the Froude number based on the orbital and cylinder diameters, respectively (see Equation 3), and a_{ow} is the water constant of proportionality between the maximum inclination of the free surface and the Froude number (a_{ow}=1.4).

$$Fr = \frac{2\pi^2 N^2 d}{g} \tag{3}$$

The hydrodynamics of shaken reactors have been indirectly investigated by Büchs et al.[4] and Klöckner et al.[13] by means of power consumption measurements in Erlenmeyer flasks and cylindrical containers, respectively. The power law correlation of the power number, Ne, of Equation 4 was obtained by Klöckner et al.[13] for different combinations of Reynolds number, Re =2400-250000, Froude number, Fr_{d_i}=0.05-0.3, orbital to cylinder diameter ratio, d_o/d_i=0.08-0.36, and non dimensional fluid volume, V_f/d_i^3 =0.08-036. This relationship is valid only for rotational speeds greater than the critical speed N_c (see Equation 5), which can be used in cylindrical OSRs to identify "suitable" shaking conditions associated with a measurable power number and in-phase flow.

$$Ne = 9\ Re^{-0.17} \left(\frac{N^2 d_o}{g}\right)^{0.42} \left(\frac{V_f}{d_i^3}\right)^{0.44} \tag{4}$$

$$N_c = \frac{1}{d_i^2}\sqrt{0.28\ V_f\ g} \tag{5}$$

Contrary to the results obtained for Erlenmeyer flasks[4], the orbital diameter was found to affect the power number in cylindrical containers.

Numerical simulation studies of the flow dynamics in shaken systems have been carried out by Zhang et al.[14] and Zhang et al.[7] for 250-ml Erlenmeyer flasks and in 24-well and 96-well bioreactors for water-like viscous fluids, respectively, while Discacciati et al.[15] developed a pressure correction method to best capture the free surface deformation and assess the shear stress levels in an orbitally shaken cylindrical container for a highly viscous aqueous solution containing 98.5 % of glycerine.

This work builds upon the mean flow transition and flow scaling law identified by Weheliye et al.[12] for fluid of water-like viscosity in a shaken cylindrical container, and aims at extending those findings to Newtonian fluids of greater viscosity. The main objective of this research is to provide improved and novel means to optimise bioprocess design and scaling in orbitally shaken reactors. This is achieved by building a flow transition map based on Re and Fr which identifies four quadrants associated to different mean flow dynamics and turbulence levels, as well as by quantifying flow characteristics such as time/length scales, shear/normal deformations and dissipation rate, which can guide the final user in the selection of the most appropriate operating conditions (N, d_o, d_i, V_f, ν) for a particular bioprocess.

2. Materials and methods

Phase-resolved PIV measurements were carried out to characterise the flow in cylindrical bioreactors of internal diameter, d_i=7, 10 and 13 cm. The cylindrical containers were made of glass and positioned inside a trough to minimise optical distortion at the cylinder wall, while the transparent bottom allowed to gain optical access from underneath the rig. The rig, a mirror, a Dantec intensified camera and a diode laser (300 mW, 532 nm) were rigidly mounted on a LS-X Kühner shaker table, with the laser and the camera being set up differently depending on whether experiments were carried out on horizontal or vertical planes of measurement (more information on the set up can be found in Weheliye et al.[12]). Experiments were obtained for fluid heights, orbital diameters and shaker speeds in the ranges of h = 3-7 cm, d_o = 1.5-5 cm and N = 60-140 rpm, respectively, while either water-glycerine mixtures, seeded with 50 μm rhodamine particles, or silicon oils, seeded with 10 μm silver coated particles, were employed to vary the fluid viscosity within the range ν=1-170$\times\nu_w$ (ν_w=10^{-6} m^{2}s^{-1}).

Synchronization of the PIV image acquisition to the orbital position of the rig was achieved by a magnetic encoder coupled to the shaker table and timing box, with the origin of the angular coordinate, ϕ, being set when the system reaches its position furthest to the left as the clockwise orbit is viewed from above. To fully resolve the large scale flow structures as well as the dissipative length scales, different sets of measurements were employed with spatial resolutions of Δx_i=-0.12-1.3 mm, while, depending on the rotational speed considered, PIV image pairs were acquired with a time interval Δt=5-10 ms. In the rest of the article a cylindrical coordinate system r, ϕ, z is employed with the origin positioned on the cylinder axis at the bioreactor base. It should be noted that in some of the plots reported in this work reference is made to negative radial coordinate, r, which, although not consistent with the cylindrical coordinate system employed, it is used here solely to discriminate between points to the left and right hand sides of the bioreactor axis. As mentioned in the introduction the Froude number based on the orbital diameter is an essential parameter to control the flow dynamics inside the bioreactor, and will be referred to here after either as Fr_{d_o} or, to simplify, as Fr.

3. Results and discussion

In the following sub-sections the four parts of the investigation, that is, extension of the flow scaling law to fluids of low viscosity (§ 3.1), mean flow characterisation for highly viscous fluids (§ 3.2, 3.3), *Fr*-*Re* flow transition map (§ 3.4), and characterisation of the flow time/length scales and turbulence properties (§ 3.5-3.8), are discussed in sequence. In brief, the rationale for the selection of these four parts of the work was to identify the range of viscosity over which the in-phase to out-of-phase flow transition determined by Weheliye et al.[12] is still valid, to assess the flow dynamics when the in-phase to out-of-phase transition occurs when highly viscous fluids are used, to map the combinations of Fr and Re delimiting the four different flow dynamics identified, and to provide flow/mixing characteristics and time/length scales that can be used to select the most appropriate operating conditions for bioprocesses with different viscosity fluids.

3.1. *Variation of free surface inclination with viscosity and extension of the flow scaling law*

Weheliye et al.[12] found a linear relationship between the inclination of the free surface and the Froude number when the working fluid was water, and this relationship was used to derive the flow scaling law of Equations 1 and 2. A similar analysis is carried out in this section to assess how the inclination of the free surface, which is the main flow driving mechanism, is affected by the viscosity of the fluid. For this study either silicon oils or different percentage mixtures of glycerine and water were employed. Three different combinations of nondimensional fluid height and orbital-to-cylinder diameter ratio are considered in Figure 1 (a), where the inclination of the free surface measured at ϕ=0° is plotted against the orbital Froude number for ν=4.97×10^{-5} m^2/s. It should be noted that similar experiments were carried out for two additional viscosities, ν=1.7×10^{-5} m^2/s and ν=1.8×10^{-4} m^2/s, which are not shown here for economy of presentation.

The current results are consistent with those obtained when water was the working fluid[12], with the data being characterised by a linear relationship between the wave height of the free surface, Δh, and the Froude number, Fr. However, the constant of proportionality, a_o, for the water/glycerine mixture of Figure 1 (a) is lower than that obtained for water[12], $a_{ow} = 1.4$. The decrease of a_o with increasing fluid viscosity was further confirmed by the experiments carried out for ν=1.7×10^{-5} m^2/s and ν=1.8×10^{-4} m^2/s, which were characterised by constants of proportionality, a_o, of 1.38 and 1.23, respectively. This behaviour is expected, as the inertial forces that push the fluid against the cylinder side wall are counterbalanced to a greater extent by the viscous forces generated by fluids of higher viscosity. From Figure 1 (a) the angle of inclination of the free surface is independent of the non-dimensional fluid height, h/d_i, and is constant for a given Froude number, Fr. This implies that the maximum inclination of the free surface is not affected by the amount of fluid volume as long as the ratio between the centrifugal and gravitational accelerations is constant. A difference worth stressing between the experiments included in this work and those reported by Weheliye et al.[12] for water is that all data points in Figure 1 (a) do not deviate from the line of reference for any Fr, implying that all the flow conditions selected for this analysis can be considered in the in-phase regime, and the shape of the free surface can be approximated to an inclined elliptic disk. This difference can be explained by considering that the range of Fr investigated in Figure 1 (a) is lower than that examined in Figure 7 (a) of Weheliye et al.[12] (i.e. $0.025 \leq Fr \leq 0.3$), where the highest end of Fr range investigated was related to a deviation from the reference line and out-of-phase flow.

The variation of the constant of proportionality, a_o, of the free surface inclination with the working fluid to water viscosity ratio, ν/ν_w, is shown in Figure 1 (b). These results show a steep variation of a_o at low viscosity ratio, with a 6% reduction of the constant of proportionality for a tenfold increase in fluid viscosity, while a further 7% reduction occurs over a wider range of $\nu/\nu_w = 10 - 180$, with a minimum value of a_o=1.225 at ν=1.8 × 10^{-4} m^2/s. The power law variation of a_o with ν/ν_w can be utilised to extend the applicability of the scaling law reported in Weheliye et al.[12] for water to fluids of higher viscosity, ν. In this case the scaling law of Equation 1 can be rewritten according to Equation 6.

$$\frac{h}{d_i} = a_{ow} \left(\frac{\nu}{\nu_w}\right)^{-0.0256} \frac{h}{\Delta h} \; Fr_{d_o} \tag{6}$$

where a_{ow} is the constant of proportionality for water.

The current flow measurements for fluids of different viscosity highlighted that the toroidal vortex structure characterising the in-phase flow of water still occurs up to a fluid viscosity of 1.7×10^{-6} m^{2}s^{-1}, and in this case Equation 6 can be used in conjunction with the critical wave amplitude (Equation 1) to determine the shaking speed associated to the in-phase to out-phase flow transition.

The velocity flow pattern and vorticity contour map obtained for two different combinations of fluid height, h/d_i=0.3 and 0.5, and ν=1.7×10^{-6} m^2s^{-1} are shown in Figures 2 (a) and (b), respectively. Similarly to the results presented in Weheliye et al. [12], the sketch above the two contour-maps shows the angular position of the cylindrical tank (blue circle) with respect to its orbit (black dashed circle), while the projection of the vertical plane of measurement is identified by the black dashed line. It should be noted that the sketch is not to scale and it is only for visualisation purposes. For both fluid heights the flow pattern is very similar to that already exhibited by water, with the two characteristic counter-rotating vortices extending towards the bottom of the tank[12]. It should be noted that according to Equation 6 the flow in the bioreactor should be relatively close to flow transition at this speed and viscosity. For example the shaking speeds predicted from Equations 1 and 6 for these two configurations, N=74.1 rpm and 95.7 rpm, are in good agreement with those, 75 rpm and 95 rpm, used for the experiments of Figures 2 (a) and (b). It can be concluded from this analysis that the extended flow scaling law of Equation 6, which identifies the flow transition from a toroidal to a whirlpool-like type of vortex, should be applied to fluids with $\nu \leq 1.7 \times 10^{-6}$ m^2s^{-1}. A detailed analysis of the flow field encountered in the cylindrical bioreactor for fluids of higher viscosity is given in the following sections.

3.2. *In-phase flow for different operating conditions with highly viscous fluids*

Based on the considerations made in the previous sections a distinction has to be made between fluids of viscosity $\nu \leq 1.7 \times 10^{-6}$ m^2s^{-1} and $\nu > 1.7 \times 10^{-6}$ m^2s^{-1}, with the first range of fluids exhibiting the toroidal vortex flow pattern encountered when water is the working fluid and thoroughly discussed in Weheliye et al. [12], while the second range of viscosity still shows an inclined free surface of elliptic shape, which is synchronised with the bioreactor position along the circular orbit, but its flow dynamics are considerably different to those observed for water. As a consequence this section aims at elucidating the flow obtained for in-phase conditions when the viscosity $\nu > 1.7 \times 10^{-6}$ m^2s^{-1}. Flow field measurements of vertical and horizontal planes were obtained for two silicon oils with viscosity, ν=1×10^{-5} m^2s^{-1} and 1×10^{-4} m^2s^{-1}.

To best compare with water data sets the reference configuration with operating conditions of h/d_i=0.3 and d_o/d_i=0.25 is considered in the vertical plane measurements of Figures 3 (a) and (b), where the phase-resolved velocity vector fields and contour plots of the tangential component of the vorticity, ω_θ, are represented for ν=1×10^{-5} m^2s^{-1} and and 1×10^{-4} m^2s^{-1}, respectively. When ν=1×10^{-5} m^2s^{-1} (Figure 3 a) the counter-rotating vortex configuration cannot be observed anymore and a different flow field is present, with the formation of a vortex region next to the right wall, below the lowest edge of the free surface, which is characterised by a vorticity of opposite direction to that experienced with water-like viscous fluids (cf. Figure 2).

This vortical structure is enhanced when the viscosity is further increased to ν=1×10^{-5} m^2s^{-1} (see Figure 3 b), as the vortex to the right hand side extends towards the centre of the tank with a maximum non-dimensional vorticity of $\frac{\omega_{\theta max}}{\pi N}$=0.8, while a less intense vorticity region also emanates from the bottom of the bioreactor. It should be noted that both the flow fields shown in Figures 3 (a, b) are characterised by a smooth inclined elliptic free surface shape, indicating that the flow is in-phase, with the maximum fluid height occurring in the vertical plane of measurement when the bioreactor is in the position furthest to the left (ϕ=0°). The flow structures and vorticity contours shown in Figures 3 (a, b) are in good agreement with those outlined by the simulations of Kim and Kizito[10], who calculated the instantaneous flow field for ν=1×10^{-5} m^2s^{-1}.

The consistency of the flow field identified in Figures 3 (a, b) for highly viscous fluids and in-phase flow was further assessed using two additional operating conditions with a different non-dimensional fluid height, h/d_i=0.38, and orbital to cylinder diameter ratio, $d_o/d_i = 0.19$, and same fluid viscosity ν=1×10^{-5} m^2s^{-1} and and 1×10^{-4} m^2s^{-1}. In this set of experiments the scalability of the flow was further tested with a larger tank reactor of cylinder internal diameter d_i=130 mm and fluid height h=5 cm. The associated contour plots are not shown here for economy of space, but all vector fields and contour plots were denoted by similar flow dynamics to those exhibited for h/d_i=0.3 and d_o/d_i=0.25 in Figure 2 (a, b) for the same viscosity and Fr, with the counter clockwise vortex at the right side wall merging with the region of positive vorticity present close to the bottom of the reactor only for ν=1×10^{-4} m^2s^{-1} (cf. Figure 3 b). It should be noted that the two regions of positive vorticity present at the side and bottom walls of the bioreactor in Figure 3 (a, b) tend to merge also if the rotational speed of the shaken bioreactor is increased, which indicates a growth in size and intensity of the main vortex present at the the right hand side wall towards the centre and bottom of the bioreactor. This implies that the single vortex flow pattern can be achieved either by increasing the viscosity, or by increasing the rotational speed of the shaken bioreactor.

The vector fields and axial vorticity contour plots in horizontal plane measurements are shown in Figures 3 (c) and (d) for ν=1×10^{-5} m^2s^{-1} and ν=1×10^{-4} m^2s^{-1}, respectively (cf Figures 3 a and b). These were obtained at an elevation of z/d_i=0.1 for analogous operating conditions to those reported in the vertical plane measurements of Figures 3 (a) and (b), with h/d_i=0.3, Fr=0.09 and d_o/d_i=0.25. Similarly to the results discussed by Weheliye et al.[12] for in-phase conditions when water was the working fluid, two in plane stagnation points denoted as A and B can be clearly distinguished in the flow fields of Figures 3 (c) and (d), with local flow diverging from stagnation point B, and converging towards stagnation point A. In this case however the two stagnation points are almost 180° apart for both the viscosities considered, while the maximum angle of separation between the two stagnation points observed for ν=1×10^{-6} m^2s^{-1} was 148° for h/d_i=0.5 and Fr=0.17 (cf. Figure 5 of Weheliye et al.[12]). Horizontal plane measurements were repeated at different elevations for both ν=1×10^{-5} m^{2}s^{-1} and ν=1×10^{-4} m^{2}s^{-1} and the characteristic flow pattern with two in plane stagnation points 180° apart was consistently present for all the heights investigated, and the different planar flow fields did not display any azimuthal angular variation, as z/d_i planes closer to the bottom of the tank were considered.

3.3. *Out-of-phase flow for different operating conditions with highly viscous fluids*

This section aims at characterising the fluid dynamics occurring in an orbitally shaken bioreactor of cylindrical geometry when the flow is in the out-of-phase regime and a fluid of viscosity ν >1.7 ×10^{-6} m^{2}s^{-1} is used. Similarly to § 3.2 flow field and free surface height measurements were obtained for two silicon oils with viscosity 10 and 100 times greater than that of water (ν=1×10^{-5} m^{2}s^{-1} and 1×10^{-4} m^{2}s^{-1}).

The out-of-phase condition has been mainly related in the literature to a phase lag of the free surface with respect to the angular position of the bioreactor along its orbit[9,4]. Based on this a free surface height analysis, analogous to that carried out for water by Weheliye et al.[12], is first made to identify a range of Fr where the out-of-phase condition is well established. The variation with phase angle, ϕ, of the non-dimensional free surface height, h_f, measured at the left hand side wall of the bioreactor for a fluid of ν =1×10^{-5} m^{2}s^{-1} is shown in Figure 4, where $h_{f_{max}}$ is the maximum free surface height obtained for a given Froude number. The reference configuration with operating conditions of h/d_i=0.3 and d_o/d_i=0.25 was used for this investigation, with measurements of h_f being repeated for three shaking speeds N=80 rpm (Fr=0.09), 90 rpm (Fr=0.11) and 105 rpm (Fr=0.15) over the entire bioreactor orbit, 0°< ϕ <360°. For Fr=0.09 and Fr=0.11 the fluid is still in phase with the bioreactor angular position, as the non-dimensional height $h_f/h_{f_{max}}$ reaches its maximum ($h_f/h_{f_{max}}$=1) at ϕ=0°, while at the highest shaking speed considered, N=105 rpm (Fr=0.15), the maximum value of h_f occurs at $\phi\approx$20°. A comparison of these results with those obtained by Weheliye et al.[12] highlights that an equivalent phase delay was obtained for water at a much larger shaking speed corresponding to Fr=0.24. This indicates that the critical Froude number, Fr_c, associated to the in-phase to out-phase flow transition becomes smaller when the fluid viscosity is increased. Similar conclusions were withdrawn by Büchs et al.[9] through power measurements of shaken flasks obtained with highly viscous fluids.

The vorticity contours and velocity vector fields for N=100 rpm and ν=1×10^{-5} m^{2}s^{-1} are shown in Figure 5. The plot exhibits a wavy profile of the free surface, while the wave amplitude, $\Delta h/d_i$, is approximately 0.18 for the Froude number considered (i.e. Fr=0.14). In Figure 5 the counter-clockwise vortical structure, already identified below the right hand side of the free surface for in-phase conditions (cf. Figures 3 a, b), is still visible, while a less intense, but larger clockwise rotating vortex is present below the concave left part of the free surface profile. It is interesting to point out how these two structures are reminiscent of the toroidal vortex present for in-phase condition when fluids of low viscosity are used (cf. Figures 2 a, b), but in this case the two vortices are rotating in the opposite direction with an axial stream flowing downwards at the centre of the bioreactor (i.e. r/d_i=0). This difference is well captured by the supporting information video, which compares dye flow visualisations obtained for a high and low viscous fluids (file name: FlowVis-different vis.avi). When the shaking frequency is increased to 110 rpm (see Figure 6 a), the two vortical structures are still visible, and characterised by similar non-dimensional vorticity intensity to that displayed at 100 rpm, while the wave amplitude $\Delta h/d_i \approx 0.21$ for $Fr = 0.17$. When comparing Figures 5 and 6 (a) it is evident that for the highest speed considered a radial stream starts to be present below the lowest side of the free surface, with fluid being pushed from the right to the left hand side of the cylindrical bioreactor. This behaviour should be attributed to the greater extent of out-of-phase occurring when the shaking speed is increased from 100 rpm to 110 rpm.

A better understanding of this phenomenon can be gained from the horizontal plane PIV measurements shown in Figure 6 (b), which are made at an elevation of z/d_i=0.1 for the same operating conditions of Figure 6 (a) (i.e. ν=1$\times$10^{-5} m^{2}s^{-1}, Fr=0.17, h/d_i=0.3, d_o/d_i=0.25). Similarly to the plots obtained for in-phase conditions (cf. Figures 3 c, d), two in-plane stagnation points are present with local flow diverging from and converging to points denoted as B and A, respectively. To best visualise the degree of out-of-phase the red and black dashed lines identify the projections of the vertical plane of measurement of Figure 6 (a), and of the vertical plane of measurement that can be associated to the smallest fluid exchange between the two counter-rotating vortical cells present at the left and right sides of the bioreactor, respectively. The latter condition occurs when the radial component of the flow on the vertical plane of measurement is minimum, and can be visualised in Figure 6 (b) by determining the orientation of the diameter which is locally orthogonal to the vector field in the largest amount of radial coordinates. For example, when the black dashed line is considered, which corresponds to the projection of the cross section of Figure 6 (a) on the horizontal plane of measurement of Figure 6 (b), the local flow exhibits a radial component, which is parallel to the black line, with fluid being moved from the right side of the bioreactor (lowest part of the free surface) to the left one (highest side of the free surface). On the contrary, the red dashed line is locally orthogonal to nearly all the vectors across the bioreactor diameter, implying that vertical plane measurements obtained at this phase angle would be characterised by two independent vortical cells with negligible fluid exchange between the lowest and highest sides of the free surface. According to this description the flow of Figure 6 (b) obtained at $\phi = 0°$ is out of phase by approximately 21°, with the left (right) side of the free surface profile moving upward (downward) if vertical plane plots were reproduced at intermediate phase angles, ϕ (i.e. $0° < \phi < 21°$).

The increase of out-of-phase delay occurring with fluid of higher viscosity is well illustrated by the velocity field and vorticity contour plots of Figures 6 (c) and (d), which were obtained with a viscosity of ν=1×10^{-4} $\mathrm{m^2s^{-1}}$ and Fr=0.14 (N=100 rpm). In Figure 6 (c) the higher viscosity induces a well established wavy profile of the free surface at a shaking frequency of N=100 rpm (Fr=0.14), while for the same Froude number the silicon oil of ν=1×10^{-5} $\mathrm{m^2s^{-1}}$ (Figure 5) just starts to exhibit an out-of-phase flow, with negligible fluid exchange between the left and right vortical cells. On the contrary the vector field of Figure 6 (c) is characterised by a strong radial stream, which moves fluid from the left side of the bioreactor to the right one, with a small recirculation present at the left corner of the cylinder cross section. This again indicates that an increase of fluid viscosity determines a lower value of the critical Froude number, Fr_c, which marks the threshold for the in-phase to out-of-phase flow transition.

As previously mentioned a strong radial jet implies a large extent of out-of-phase flow, and this is well exemplified in Figure 6 (d), where horizontal plane measurements are presented for the same operating conditions as those of Figure 6 (c) (i.e. ν=1×10^{-4} $\mathrm{m^2s^{-1}}$, Fr=0.14, h/d_i=0.3, d_o/d_i=0.25). For this viscosity the out-of-phase flow condition is clearly evident with the imaginary line connecting the two stagnation points being at an angle with respect to the black dashed line indicating the position of the vertical plane of measurement at a phase angle $\phi = 0°$. Similarly to the analysis carried out for ν=1×10^{-5} $\mathrm{m^2s^{-1}}$ (cf. Figure 6 b), the red dashed line of Figure 6 (d) is locally orthogonal to the vector field, and visualises the projection on the horizontal plane of the vertical plane of measurement that would exhibit two distinct vortical cells. For this combination of viscosity, Froude number and non-dimensional height the flow is out of phase by 41°. Horizontal plane measurements were repeated at different elevations for the two silicon oils with viscosity of ν=1×10^{-5} $\mathrm{m^2s^{-1}}$ and ν=1×10^{-4} $\mathrm{m^2s^{-1}}$, and the corresponding contour and vector plots showed that the extent of out-of-phase flow is constant throughout the fluid height range.

To further assess the variation of the flow dynamics in the out-of-phase flow regime of highly viscous fluids, two additional configurations were investigated with a non-dimensional fluid height of h/d_i=0.5 for ν=1×10^{-5} $\mathrm{m^2s^{-1}}$ and ν=1×10^{-4} $\mathrm{m^2s^{-1}}$ and are shown in Figures 7 (a) and (b), respectively. The velocity vector and vorticity contour plots of Figure 7 (a) exhibit a flow pattern similar to that of Figure 5, with two clear counter-rotating vortices at the sides of the measurement cross section. The fact that the two vortices are discernible and nearly completely separated implies that at this Fr the flow is out-of-phase by a small phase angle. From this point of view it is interesting to note that for a fluid height of $h/d_i = 0.3$ the two counter-rotating vortices were completely distinct for Fr=0.14, while at fluid height of $h/d_i = 0.5$ a similar condition occurs at a greater speed corresponding to Fr=0.2. This behaviour is analogous to that already described for low viscous fluids by Weheliye et al.[12], where it was found that transition to out-of-phase flow is retarded when the non-dimensional fluid height is increased. In agreement with previous results for ν=1×10^{-4} m^{2}s^{-1}, the vorticity contour and velocity vector maps of Figures 7 (b) are characterised by a strong radial jet pushing fluid from the right side of the bioreactor towards the left one, implying that for these operating conditions, h/d_i=0.5 and Fr=0.15, the flow is out-of-phase by a large amount, close to that exhibited for a non-dimensional fluid height of $h/d_i = 0.3$ at Fr=0.14 (cf. Figures 6 c, d).

The current section highlighted that the flow dynamics for out-of-phase flow are different for fluids of high and low viscosity, with a precessional vortex dominating the flow for $\nu \leq 1.7\times10^{-6}$ m^{2}s^{-1} (see Weheliye et al.[12]), and two vortical cells with an azimuthal axis characterising the flow for $\nu > 1.7\times10^{-6}$ m^{2}s^{-1} (cf. Figures 5, 6a and 7a). Moreover it was found that an increase in fluid viscosity promotes out-of -phase flow, while an increase of fluid height increases the critical Fr_c associated to the flow transition.

3.4. ***Flow map for different*** Re ***and*** Fr

A summary of the different flow regimes encountered in an orbitally shaken bioreactor of cylindrical geometry for different operating conditions is provided in the *Re*-Fr flow map of Figure 8. It should be noted that the plot was made for the reference non-dimensional fluid height, h/d_i=0.3. The flow map of Figure 8 is based on the Froude number definition of Equation 3 using the orbital diameter as characteristic length scale, while *Re* is defined in Equation 7.

$$Re = \frac{\pi N d_o \, d_i}{\nu} \tag{7}$$

It should be noted that other definitions of *Re* can be found in previous works on orbitally shaken bioreactors, such as those of Büchs et al.[4] (see Equation 8) and Kim and Kizito[10] (see Equation 9), which are both based on the cylinder diameter.

$$Re = \frac{N {d_i}^2}{\nu} \tag{8}$$

$$Re = \frac{\pi N {d_i}^2}{2\,\nu} \tag{9}$$

In the current work the definition of Equation 7 was selected because it is evident from the scaling law derived by Weheliye et al.[12], and from the analyses carried out for high viscosity fluids in the previous sections, that the reference speed should be based on the orbital motion (cf. $V = \pi N d_o$), and this is also confirmed by the relevance of the orbital Froude number on the flow transition, while the characteristic length scale should be associated to the inner cylinder diameter, which induces for low viscous fluids the flow transition to a precessional vortex because it is directly linked to the wall curvature.

The *Re*-Fr map of Figure 8 can be subdivided into four regions denoted by upward/downward arrows to discriminate between high and low values of Froude and Reynolds numbers. The vertical dashed line differentiates between fluid of low viscosity (i.e $\nu \leq 1.7\times10^{-6}$ m^{2}s^{-1} and high

Re), where the flow is dominated either by a toroidal vortex with an upward central stream for in-phase conditions (i.e. low Fr, right-bottom quadrant), or by a precessional vortex of vertical axis for out-of-phase conditions (i.e. high Fr, right-top quadrant), and fluid of high viscosity (i.e. $\nu > 1.7 \times 10^{-6}$ m^{2}s^{-1} and low *Re*), where the in-phase flow is characterised by a single vortex formed below the lowest side of the free surface spreading towards the bottom of the bioreactor (i.e. low Fr, left-bottom quadrant), or by a toroidal vortex with a downwards central stream and a wavy free surface profile for out-of-phase conditions (i.e. high Fr, left-top quadrant). To improve the readability of the figure a visual representation of the different flows occurring for the four combinations of *Re*-Fr can be gained from the vertical and horizontal plane insets of Figure 8. Several conditions with varying h, d_o, d_i, N and ν are reported in Figure 8 (d_o/d_i=0.11-0.71, ν/ν_w =1-100, h/d_i=0.3), where empty and filled symbols discriminate between in-phase and out-of-phase flows, respectively.

To put the results of the flow map of Figure 8 into context, a list of the operating conditions most commonly selected for cultivation of mammalian cells is reported Table 1. Beside the selected operating speeds, Table 1 indicates the transitional shaking speed that can be predicted from the scaling law obtained of Equation 1, for each work mentioned in the table. From these results it is evident that mammalian cells are mainly cultivated in the out-of-phase regions (i.e. right-top quadrant of Figure 8). It is worth to stress that the map shown in Figure 8 was obtained for a constant non-dimensional height, h/d_i=0.3, and comparison with the data of Table 1 should be made with care.

Ref.	h/d_i [-]	N [rpm]	N_c [rpm]	*Re* [-]	Fr [-]	d_o/d_i [-]	**Flow condition**
Zhang et al.[16]	0.38-0.75	110	72-86	49.5×10^3	0.34	0.29	out-of-phase
Tissot et al.[17]	0.42-0.98	90	66	68×10^3	0.23	0.17	out-of-phase
Klöckner et al.[13]	0.11-0.54	60-120	34-66	$45\text{-}90\times10^3$	0.10-0.40	0.17	out-of-phase

Table 1: Flow conditions commonly selected for mammalian cell cultivation.

The following sections aim at elucidating the variation of the circulation, turbulent kinetic energy and normal/shear rates when different points across the *Re*-Fr map are considered, and at gaining a better understanding of the implications of the different in-phase and out-of-phase flow transition occurring at different *Re* for bioprocess design.

3.5. *Kinetic energy variation with flow regime*

In this section the turbulent kinetic energy of the flow is investigated for different combinations of Fr and Re. The turbulent kinetic energy content was estimated according to the 2D approximation of Equation 10, where the asterisk denotes the space average of $\sqrt{\langle u_r'^2\rangle + \langle u_z'^2\rangle}$ over the entire vertical plane of measurement, while the angle brackets denote a phase resolved average. It should be noted that the dimensions of $\sqrt{\langle u_r'^2\rangle + \langle u_z'^2\rangle}^*$ are m/s, and therefore it should be considered as a reference velocity of the kinetic energy due to turbulent fluctuations, and here after will be referred to as turbulent kinetic energy reference velocity. The data reported in this section refers to a phase angle $\phi = 0°$.

$$\left(\sqrt{\langle u_r'^2\rangle + \langle u_z'^2\rangle}\right)^* = \frac{1}{A}\int_A \left(\sqrt{\langle u_r'^2\rangle + \langle u_z'^2\rangle}\right) dA \tag{10}$$

Estimates of the turbulent kinetic energy content for increasing Fr are reported in Figure 9 (a) for three different constant Reynolds numbers, Re=9163, 13090 and 17017. According to Equations 3 and 7, the Froude number was increased by increasing the shaken rotational speed, while the Reynolds number was kept constant by ensuring a constant product between the shaken rotational speed and the orbital diameter, $N \times d_o$. This implies that each data point aligned along a vertical line in Figure 8 correspond to different orbital to cylinder diameter ratios (d_o/d_i=0.11-0.71). To assess thoroughly the relevance of Re on the turbulent kinetic energy content, data sets of Re=9163 and 13090 were repeated twice using for each data set two different combinations of ν and d_i such that d_i/ν was constant. This experimental methodology can be better understood from the definition of Re of Equation 7, where it is evident that for a given Fr (i.e. fixed combination of N and d_o), the same Re can be achieved by varying ν and d_i such that their ratio d_i/ν is constant. For example, the same flow regime of $Re = 9163$ was obtained either by using water (ν_w) in a cylinder of diameter d_i=70 mm or a water-glycerine mixture (ν_w=1.4) in a cylinder of diameter d_i=100 mm, such that in both cases $d_i/\nu \approx 70/\nu_w$. It is worth noting that according to the experimental methodology employed data points corresponding to fixed values of Re and Fr are all obtained for a constant orbital diameter, d_o, independently of the viscosity considered.

An indication of the five sets of data used to assess the variation of the turbulent kinetic reference velocity against Fr is provided on the Re-Fr map in Figure 8, to the right of the dashed line discriminating between high and low viscous fluids, where the different data points are aligned along vertical lines of constant Re. It should be noted that in Figure 8 data sets obtained for the same Re would have overlapped, and therefore to improve the readability of the figure data associated to $\nu > \nu_w$ are shifted slightly to the right. The distinction between empty and filled symbols highlights that even at the same Re transition to out-of-phase flow occurs at different Fr for different viscosities.

The variation of $\frac{\left(\sqrt{\langle u_r'^2\rangle + \langle u_z'^2\rangle}\right)^*}{\pi N d_o}$ is plotted against Fr in Figure 9 (a). For all the different Re considered the turbulent kinetic energy content is negligible at low values of Fr, as all the data sets are in the in-phase flow regime. Two main points can be made from Figure 9 (a):

1. The increase of the turbulent kinetic energy occurs at different transitional Fr, with data sets associated to a greater Re undergoing the out-of-phase transition at a lower Fr. For example at $Fr = 0.2$, data associated to $Re = 17017$ and 13090 (ν_w, $d_i = 130$ mm) already exhibit a non-dimensional turbulent kinetic energy reference velocity of 48%, while for the lowest Re considered $\frac{\left(\sqrt{\langle u_r'^2\rangle + \langle u_z'^2\rangle}\right)^*}{\pi N d_o} \approx 10\%$.
2. The turbulent kinetic energy content is different even when the same Re is considered. This aspect is clearly present when comparing the data sets for Re=13090 (empty circles and red triangles) and 9163 (filled squares and blue triangles). For example at Fr=0.18 water data exhibit a $\frac{\left(\sqrt{\langle u_r'^2\rangle + \langle u_z'^2\rangle}\right)^*}{\pi N d_o}$ of 20% and 6% at Re=13090 and Re=9163, respectively, while for analogous Re water-glycerine mixtures are denoted by values of the turbulent kinetic energy reference velocity of 37% and 20%.

This behaviour can be explained by considering that according to Equation 6 and to the critical wave amplitude, $(\Delta h/h)_c$, of Equation 1, transition to out-of-phase flow in the high Re range will occur at a lower speed (i.e. lower Fr) for a less viscous fluid and/or for a cylinder of larger internal diameter. From this point of view, contrary to the data of Figure 9 (a), water-glycerine mixtures should exhibit lower turbulence levels than those reported for water at analogous Re, because flow transition should occur at a higher transitional Fr_c than water. However, it should be stressed that in order to keep Re constant water-glycerine mixture experiments were carried out in larger cylinders than those used for water, implying that flow transition should occur in these geometries at a lower transitional Fr_c than water. From the greater turbulence levels exhibited by the water-glycerine mixture data at analogous Re, it is clear that the fluid viscosity has a lower impact on the transitional Froude number, Fr_c, than the cylinder diameter d_i when $\nu \leq 1.7\times10^{-6}$ m^{2}s^{-1}.

To take into account the difference in transitional Fr_c due to the different selection of viscosity and cylinder diameter, the five data sets of Figure 9 (a) are replotted in Figure 9 (b) using the ratio Fr/Fr_c. From this figure the advantages of employing the ratio Fr/Fr_c are evident, as all the data sets tend to collapse on each other irrespective of the Re, and a single curve can be identified, aiding a more effective scaling of the turbulent kinetic energy between cylindrical bioreactors of different sizes and employing different working fluids. These results help to explain the findings of Rodriguez et al.[18], who compared mixing time data obtained in different laboratories for cylindrical bioreactor of different sizes and operating in different conditions, and concluded that bioreactors mixing performances can be scaled if the mixing number NT_m, is plotted against Fr/Fr_c. Their data show that mixing number is nearly constant for $Fr/Fr_c \geq 1.4$, indicating that for these flow regimes mixing dynamics are mainly controlled at a local scale by turbulent eddies.

The variation of the turbulent kinetic energy reference velocity with Re is plotted for two constant Froude numbers selected in the in-phase flow regime ($Fr = 0.11$) and the out-of-phase one ($Fr = 0.17$), respectively, in Figure 10. These two Fr conditions are visualised by the two horizontal data sets at $Fr = 0.11$ and 0.17 in Figure 8. It should be noted that the two lines cross the vertical dashed line discriminating between flow conditions of high and low viscous fluids and identifying different types of flow patterns both for in-phase and out-of-phase conditions. It has to be stressed that for these data sets Re was varied by changing the fluid viscosity, ν. At Fr =0.11 turbulence levels are extremely low and hardly vary with increasing Re. This indicates that, despite the differences in mean flow pattern, the flow regimes occurring for in-phase conditions both for high and low viscous fluids are laminar, with negligible turbulent fluctuations. When $Fr = 0.17$ is considered the turbulent kinetic energy reference velocity is close to 5% of the orbital velocity at the lowest Re considered (i.e. most viscous fluid), indicating that some chaotic fluctuations already occur for out-of-phase condition of high viscous fluids. The intensity of $\sqrt{\langle u_r'^2 \rangle + \langle u_z'^2 \rangle}$ shows a relatively low growth for $Re < 2000$, while a steeper increase occurs thereafter as the dashed vertical line is approached and the out-of-phase flow starts to exhibit the precessional vortex characterising low viscosity fluids. For the highest Re considered the turbulent kinetic energy content is more than 20% of that associated to the orbital shaken motion.

3.6. *Strain rate tensor*

Recent studies have shown that “shear sensitivity” should not be considered a major concern for growth of animal cells in suspension[19,20], but might play a role when microcarriers and anchorage-dependent animal cells are considered, as the stresses could potentially remove the cell attached to the microcarrier surface[21,22]. Morevover there is a growing interest in understanding the effect of shear stress on stem cells and cells for therapy, and the low shear levels present in OSRs could potentially make this device a suitable option for scaling up cell expansion using suspension cultures[23]. From this point of view operating conditions should be carefully selected by comparing the Kolgomorov length scale to the size of the microcarriers or cell aggregates[24]. Based on these considerations this section and the following one aim at providing an estimate of the strain rate tensor and dissipation rate occurring in an orbitally shaken bioreactor.

The evaluation of the shear rate magnitude and the identification of high shear zones in the bioreactor are important aspects of bioprocess design, as they directly affect the viability of the cell culture. High shear stress can disrupt the cell membrane, leading to cell death. In this section a 2D analysis of the phase resolved strain and shear rates occurring in the vertical plane of measurement is carried out. The 2D phase resolved rate of strain tensor is defined in Equation 11:

$$\boldsymbol{S}_{ij} = \begin{pmatrix} 2\,\frac{\partial\langle u_r\rangle}{\partial r} & \left(\frac{\partial\langle u_r\rangle}{\partial z} + \frac{\partial\langle u_z\rangle}{\partial r}\right) \\ \left(\frac{\partial\langle u_r\rangle}{\partial z} + \frac{\partial\langle u_z\rangle}{\partial r}\right) & 2\,\frac{\partial\langle u_z\rangle}{\partial z} \end{pmatrix} \tag{11}$$

where S_{rr}, S_{zz}, are the radial and axial strain rates, while S_{rz} is the shear rate. It should be noted that positive (negative) values of the strain rates (i.e. S_{rr}, S_{zz}) correspond to local stretching (compression) of the fluid element.

The variation of the strain and shear rates, S_{rr}, S_{zz} and S_{rz} of the phase-resolved flow with Froude number, Fr, are shown in Figures 11 (a), (b) and (c), respectively. Two sets of data with different cylinder diameter and viscosity but same Re are presented. As reported in Equation 12 the asterisk denotes the space average of the absolute value of S_{ij} over the entire vertical plane of measurement.

$$|S_{ij}|^* = \frac{\int_A |S_{ij}| dA}{A} \tag{12}$$

The results of Figure 11 (a-c) show a similar behaviour for the different $|S_{ij}|^*$ considered with a nearly linear increase of the strain and shear rates with Fr for both the two Re data sets. The axial strain and shear rates are denoted by a higher magnitude over the range of Fr considered ($|S_{zz}|^*$=$|S_{rz}|^*$=0-1.4πN), while the space averaged radial strain rate, $|S_{rr}|^*$, does not exceed 1πN for any Froude number.

The local normal and shear rates were found to be highest close to the cylinder wall, with values of the normal strain rates in the radial and axial directions and shear rate being $|S_{rr}|$=2πN, $|S_{zz}|$=1πN and $|S_{rz}|$=3.5πN, respectively. The maximum dimensional shear stress, based on the principal components of the deformation rate tensor, is τ_{ij}= 0.022 Nm^{-2}, where i and j indicate the local directions (eigenvectors) of the principal strain rate components. This value is significantly lower than those affecting cells, and for example the review by Eliase et al.[25] reported that mammalian cells are usually damaged by shear stresses above 0.15 Nm^{-2}. As mentioned earlier, robust animal cells growth in suspension are not damaged by shear levels experienced in STRs even at high impeller rotational speed[19]. It should be stressed however that the values of Figure 11 (c) are phase-resolved shear stresses, and instantaneous shear stresses could potentially be characterised by higher fluctuations, closer to the critical threshold identified by the work of Eliase et al.[25].

3.7. *Rate of viscous dissipation of turbulent kinetic energy and Kolmogorov scale*

The rate at which transport processes occur in the bulk of the liquid is highly dependent on the volumetric power consumption and on the distribution of the viscous dissipation rate of kinetic energy, ϵ, within the bioreactor. For example, Zhang et al.[7] report that liquid mixing and oxygen transfer rates of a shaken bioreactor are critically affected by both the volumetric power consumption and local levels of viscous dissipation rate of kinetic energy. Although accurate estimates of the local dissipation rate, ϵ, have been obtained in stirred tank reactors, either by direct measurements of the velocity gradients, Baldi and Yianneskis[26], Ducci and Yianneskis[27], or indirectly from the kinetic energy balance equation, Escudié and Liné[28], no such information is available for cylindrical shaken bioreactors.

In this work the viscous dissipation rate of kinetic energy was estimated from Equation 13, which has been previously employed by Sharp and Adrian[29] to measure ϵ in a vessel stirred by a Rushton turbine, and is based on the assumption of statistical isotropy for the velocity gradients and cross product term that cannot be directly estimated with 2D-PIV[26,29].

$$\epsilon = \nu \left[2\left(\frac{\partial u_r}{\partial r}\right)^2 + 2\left(\frac{\partial u_z}{\partial z}\right)^2 + 3\left(\frac{\partial u_z}{\partial r}\right)^2 + 3\left(\frac{\partial u_r}{\partial z}\right)^2 + 2\left(\frac{\partial u_r}{\partial z}\frac{\partial u_z}{\partial r}\right) \right] \tag{13}$$

According to the simulations of Zhang et al.[14] and Zhang et al.[7] most of the kinetic energy in shaken flasks and microwells is dissipated at the bioreactor walls. Therefore, in order to correctly estimate the velocity gradients at the walls, the PIV measurements obtained within the bioreactor were combined with boundary conditions to impose a zero velocity ($u_r = u_\theta = u_z = 0$) in all locations at z/d_i=0 or r/d_i=0.5.

The distribution inside the bioreactor of the viscous dissipation rate of kinetic energy for h/d_i=0.3, $\phi = 270°$, Fr=0.11 (N=90 rpm) and d_o/d_i=0.25, is shown in Figure 12 (a). In agreement with the simulations of Zhang et al.[14] and Zhang et al.[7] obtained for different types of bioreactor, it is evident that for a shaken cylinder the largest amount of kinetic energy is also dissipated near the walls, with a three orders of magnitude difference between the local dissipation rate in the bulk of the flow and at the walls. It should be noted that the flow field at this ϕ exhibits a strong radial flow, with movement of fluid from one side of the bioreactor to the other one[12]. For $\phi = 270°$ the highest energy is dissipated at the right wall with the maximum reaching 330, while the energy dissipated at the free surface is not as high ($\frac{\epsilon}{\nu(\pi N)^2} \approx$70).

An analysis was carried out to assess to what extent the measurement spatial resolution, Δx_i, affects the estimate of the dissipation rate, and to compare the measurement spatial resolution against the Kolgomorov scale. The analysis was obtained for in-phase flow conditions, when the toroidal vortex is fully developed. Two different phase angles were considered that are most representative of the flow in the cylindrical bioreactor: $\phi = 0°$, when the free surface reaches its maximum inclination, and $\phi = 270°$, when the free surface profile is horizontal on the plane of measurement. Four different sets of experiments were made with decreasing interrogation area, 10×10 cm^2, 4×4 cm^2, 3×3 cm^2, 2×2 cm^2 and 1×1 cm^2 close to the left wall of the cylindrical bioreactor, and increasing spatial resolution, $\Delta x_i/d_i$=0.013, 0.005, 0.0037, 0.0025 and 0.0012. To compare in a consistent manner the different spatial resolution sets of measurement, the dissipation rate, ϵ^*, was averaged according to Equation 14, over the area A_s which is in common to all the interrogation windows considered. The area, A_s, was 1 cm high and twice the spatial resolution, Δx_i, of each set of experiment in the horizontal direction.

$$\epsilon^* = \frac{1}{A_s}\int_{A_s} \epsilon \, dA_s \tag{14}$$

Figure 12 (b) shows the variation of the non-dimensional ϵ^* with decreasing Δx_i for h/d_i=0.3, Fr=0.11, d_o/d_i=0.25. From Figure 12 (b), it can be seen that the average energy dissipation, ϵ^*, increases as the window size of the flow field is reduced. The influence of the spatial resolution on ϵ^* can be explained by the strong dependence of the velocity gradient estimation on the distance between two adjacent measurement locations. The estimates of ϵ^* show small differences at low spatial resolutions ($\frac{\Delta x_i}{d_i} > 5\times10^{-3}$), while they differ significantly at higher spatial resolutions ($\frac{\Delta x_i}{d_i} < 5\times10^{-3}$). In the latter case, a small change in spatial resolution produces significant variations in the value of the estimated ϵ^*. Furthermore it should be noted that a higher ϵ^* is observed for ϕ=270°, which is almost double that obtained for ϕ=0° when the finer resolution is considered ($\frac{\Delta x_i}{d_i} = 1.2\times10^{-3}$). This behaviour is expected since the dominating velocity component for ϕ=0° at the outer regions of the cylinder is u_θ, which is approximately three times greater than the other two velocity components u_r and u_z. This implies that for this phase angle it is not possible to extract from the 2D PIV measurement, the term $(\partial u_\theta/\partial r)^2$ which is most likely to account for the largest amount of energy dissipation at $\phi = 0°$. On the contrary for ϕ=270° the main velocity components lie on the plane of measurement, with u_z being the greater component in the region, next to the wall, of maximum energy dissipation.

The variation of ϵ^* with increasing Fr is assessed in Figure 12 (c). For this analysis the highest spatial resolution achievable, $\frac{\Delta x}{d_i} = 1.2\times10^{-3}$, corresponding to an interrogation window of 1×1 cm^2, is employed for h/d_i=0.3, ϕ=270° and d_o/d_i=0.25. The results of Figure 12 (c) show that the average energy dissipation, ϵ^*, increases significantly with increasing Fr, as the non-dimensional ϵ^* varies between 50-1800 over the range of Fr considered. According to the measurements of Rodriguez et al.[30] the kinetic energy content of the phase-resolved flow increased by two orders of magnitude with Froude number varying in the range of Fr=0.05-0.15, while for the same Fr range the contribution due to the random velocity fluctuations, k'^*_{rz}, was nearly negligible ($k'^*_{rz} << 10^{-2}(\pi N d_o)^2$). This implies that at this low Fr regime turbulence is not yet developed, and therefore the kinetic energy is mainly dissipated by the viscous stresses generated by the large scale flow structures (toroidal vortex) next to the cylinder wall.

Another important parameter that has to be considered in the design of a bioprocess is the Kolmogorov length scale, η_k, which indicates the size of the eddies dissipating most of the kinetic energy, and should be compared to the size of the cultivated cells and/or micro-carriers to establish whether local viscous stresses could potentially determine cell damage. The definition of η is given in Equation 15.

$$\eta_k = \left(\frac{\nu^3}{\epsilon}\right)^{1/4} \tag{15}$$

with ϵ being the rate of viscous dissipation of kinetic energy, and ν the fluid kinematic viscosity. It has to be stressed that the Kolmogorov length scale and its definition of Equation 15 are generally used in turbulent flow, and recent studies on grid turbulence flows have shown that Kolgomorov scaling still holds at relatively low Reynolds number based on the Taylor length scale, $Re_\lambda \geq 25$ (see Kamruzzaman et al.[31]). In the present work values of $Re_\lambda = u' \ \lambda/\nu \approx 1.9$ and ≈ 1.45 based on the radial Taylor length scale were found in proximity of the wall, where most of the energy is dissipated, and in the bulk flow of the cylinder, respectively, at $N = 90$ rpm, when flow transition starts to occur, but these values will increase at higher speeds when turbulence builds up (see Figures 9). Taking into account these limitations the current data can provide a first estimate of the dissipative length scales, which are necessarily present also in a laminar flow. The variation of the dissipative length scale, η_k, with increasing Froude number, is shown in Figure 12 (d). Similarly to the dissipation rate results of Figure 12 (c), the data presented in Figure 12 (d) were obtained for the highest spatial resolution, $\frac{\Delta x}{d_i}$=1.2×10^{-3}. From the variation of η_k with Fr (Figure 12 d), it is observed that for the lower shaking frequency analysed, N=60 rpm (Fr=0.05), a large normalized dissipative length scale, $\frac{\eta_k}{di}$=1×10^{-3} is observed, whereas for the greater speed considered, N=100 rpm (Fr=0.14), the dissipative length scale is $\frac{\eta_k}{di}$= 5×10^{-4}. This analysis indicates that both the measurement spatial resolution and the Froude number, Fr, have a great impact on the estimated size of the dissipative eddies, and careful selection of the spatial resolution, especially at high Fr, should be sought to produce reliable results that can advise on bioprocess design.

To further assess the current measurements of the dissipation rate of kinetic energy, and to compare with the results available in the literature, the volumetric power consumption, P_v, was estimated from the volumetric integral of ϵ reported in Equation 16. In agreement with results of Figure 12 (a), the integral was limited only to the regions next to the bottom and side walls, using the maximum possible spatial resolution, $\frac{\Delta x}{d_i}$=1.2×10^{-3}. To take into account the three dimensionality of the system, the measurements were carried out over the entire range of phase angles with a 10° increment. The discrete integration was made in a cylindrical coordinate system and carried across trapezoidal elements with sides $\Delta\phi$=10°, and $\Delta z = \Delta r$=1.2×10^{-4} m.

$$\frac{P}{V_f} = \frac{\int_{V_f} \rho \ \epsilon \ dV_f}{V_f} \tag{16}$$

Using this methodology the volumetric power consumption was estimated to be P_v=45.6 W/m^3. The order of magnitude of the current results compares reasonably well with those of Klöckner et al.[13], who estimated P_v in a shaken cylinder by means of torque measurements, and found for similar operating conditions ($d_o = 2.5$ cm, V_f=6 l) values of P_v =50-200 W/m^3 for shaking speeds of 90-130 rpm.

3.8. *Circulation time*

A further analysis was carried out to asses how the circulation of the toroidal vortex varied with the phase angle, ϕ. The non-dimensional circulation time, NT^*, was estimated from the inverse of the average vorticity obtained from Equation 17, where the integral is carried out over the area, A_ω, corresponding to a vorticity level greater than a fixed threshold.

$$\omega_i^* = \frac{\int_{A_{\omega^\star}} \omega_i \; dA_i}{A_{\omega^\star}} \tag{17}$$

The variation of the non-dimensional ensemble-averaged circulation time, $N\overline{T}^*_{\omega\theta=0.1}$, with Fr and h/d_i is provided in Figure 13 (a). As expected the circulation time is decreasing for increasing Fr, as the strength of the toroidal vortex increases in magnitude for greater values of the shaking frequency, N. Moreover it is worth to point out that lower h/d_i corresponds to shorter circulation time, implying that advection is greater for those operating conditions, and enhanced mixing could be expected. This is indeed confirmed by the mixing time measured by Tissot et al.[17] who found that for decreasing fluid volume and increasing N the mixing time in a cylindrical shaken bioreactor becomes shorter. In Figure 13 (a) the circulation time at Fr=0.11 for a non-dimensional fluid height h/d_i=0.3 is rather lower than those of the other two heights investigated. This may be explained by considering that at this Fr the flow for this liquid height starts being out-of-phase and therefore different flow dynamics are experienced in the bioreactor[12].

The variation of the vortex circulation time, NT^*, was further investigated for different orbital to cylinder diameter ratios, d_o/d_i. Contrary to the results of Figure 13 (a), the data of Figure 13 (b) were obtained from phase-resolved velocities for a fixed non-dimensional fluid height, h/d_i=0.3, and phase angle $\phi = 0°$. The phase-resolved circulation time was estimated from the inverse of the space averaged vorticity of Equation 17 using a non-dimensional vorticity threshold, $\frac{\omega_\theta}{\pi N} = 0.3$. The data presented in Figure 13 (b) are related to transition to incipient flow, when the toroidal vortex extends to the bottom of the bioreactor. From the scaling law reported in section 1 this implies that all the combinations (d_o, d_i) analysed satisfy the condition $h/d_i<(d_o/d_i)^{0.5}$. From Figure 13 (b) the non-dimensional circulation time associated to transition to incipient out-of-phase flow decreases with increasing d_o/d_i. This behaviour is in agreement with the discussion made by Weheliye et al.[12], where it was found that the critical wave amplitude $(\Delta h/h)_c$ increases with increasing d_o/d_i. In fact greater $(\Delta h/h)_c$ implies greater inclination of the free surface and therefore a greater transitional Froude number, Fr_c, which is associated to a toroidal vortex of greater strength and therefore shorter non-dimensional circulation time. These results compare very well with the mixing time measurements of Tissot et al.[17], who showed that for increasing d_o the mixing time decreased. The implications of these results are potentially useful for the selection of optimum d_o, d_i and N for the design of bio-processes where an in-phase flow is preferable without reducing mixing and cell suspension performances.

In the previous part the study focussed on circulation times obtained from the tangential vorticity, ω_θ, which is the most significant component before transition to out-of-phase flow, when the fluid dynamics in the bioreactor is dominated by a toroidal vortex. In the following an analysis of the secondary circulation time based on the axial vorticity component, ω_z, for in-phase conditions is performed. The circulation time was estimated from the average vorticity of Equation 17, where the integration was carried out over regions corresponding to $\omega_z/(\pi N) \geq 0.1$. The size of the integration regions varied depending on the horizontal plane of measurement considered, as these could be either in the "convection" or "diffusion" zones depending on the Froude number and on the non-dimensional fluid height considered[17,12]. Figure 13 (c) shows the variation of the circulation times at different axial planes for two non-dimensional fluid heights, h/d_i=0.5 and 0.7 and fixed Froude number, Fr=0.11 (N=90 rpm). To better compare the axial circulation times obtained for the different fluid heights investigated a non-dimensional axial coordinate, $(h-z)/d_i$, with origin on the free surface at rest has been considered. This implies that horizontal planes located closer to (further away from) the free surface are associated to lower (higher) values of $(h-z)/d_i$ in Figure 13 (c). This normalised coordinate is consistent with the results reported in Weheliye et al.[12], where the same shaking speed was associated to analogous penetration heights of the toroidal vortex towards the bottom of the tank, and therefore analogue sizes of the "convection zone" for the two non-dimensional fluid heights considered, h/d_i=0.5 and 0.7. This analogy is well exemplified in Figure 13 (c), where the circulation time is approximately denoted by similar intensity irrespective of the fluid height considered at a given distance from the free surface. It is worth to point out that the circulation time obtained from the axial vorticity is smaller (larger) in the diffusion (convection) zone, resulting in a longer time for a fluid parcel to complete a loop around the vertical axis of the bioreactor in the region dominated by the toroidal vortex. This behaviour can be explained by looking at the horizontal flow fields at different heights of Weheliye et al (cf Figure 5a of Weheliye et al.[12]), and considering that those in the "diffusion" zone are mainly characterised by solid body rotation and therefore associated to higher values of the axial vorticity and reduced axial circulation times than those in the "convection" zone.

The variation of the azimuthal circulation time, $NT^*_{\omega\theta=0.1}$, with Fr is assessed in Figure 13 (d) for fluids of viscosity higher than water, $\nu = 10 \times \nu_w$ and $\nu = 100 \times \nu_w$. In both cases the viscosity is $\nu > 1.7\times10^{-6}$ m^{2}s^{-1}, and the flow transition described in §3.2 and §3.3 for high viscous fluids should be considered. The average vorticity ω^*_θ was obtained from Equation 17, where the area used to carried out the integration is enclosed by the contour of the selected vorticity threshold $\omega_\theta/(\pi N)$=0.1. When comparing the results of the two viscosities considered in Figure 13 (d), it is evident that the circulation time drops with decreasing fluid viscosity, with $NT^*_{\omega\theta=0.1}$ varying over the same range of $Fr = 0.07 - 0.14$ between 0.53-1.67 and 0.74-2.12 for $\nu = 1\times10^{-5}$ m^{2}s^{-1} and $\nu = 1\times10^{-4}$ m^{2}s^{-1}, respectively. As expected the circulation times are greater than those reported for water in Figure 13 (b), which varied in a range NT^*=0.5-0.9.

4. Conclusions

The results presented in this work shed light on the flow dynamics of shaken bioreactors and on the influence of critical non-dimensional operating parameters on the transport phenomena of such vessels. Flow characteristics, such as circulation time, vortex size, viscous dissipation rate, interfacial area and strain/shear rates can improve process design methodologies and help guide the selection of optimal operating conditions to enhance mixing performances.

The variation of the free surface angle against Fr was investigated for different working fluids, and a power law that correlates the constant of proportionality, a_o, and the fluid viscosity was determined (cf. Figure 1). This allowed to extend the flow scaling law derived by Weheliye et al.[12] to fluids of viscosity higher than water (cf. Equation 6). A thorough analysis of the phase resolved flow fields occurring in an orbitally shaken bioreactor of cylindrical geometry was then carried out, and it was found that the in-phase and out-phase flow characteristics associated to toroidal and precessional vortices, respectively, did only occur for fluids of low viscosity with $\nu \leq 1.7\times10^{-6}$ $\mathrm{m^2s^{-1}}$ (cf. Figures 2). The in-phase flow of fluids of higher viscosity was characterised by a vortical structure observed below the lowest side of the free surface and extending towards the bottom of the tank with increasing Fr (cf. Figure 3). On the contrary a toroidal vortex with a central downward stream is formed below the wavy free surface when the flow is out-of-phase and $\nu > 1.7\times10^{-6}$ $\mathrm{m^2s^{-1}}$ (cf. Figure 5). Measurements on horizontal planes allowed to determine the degree of out-of-phase occurring for different fluid viscosity. It was found that viscosity significantly promotes out of phase transition, with the flow of silicon oils of $10\nu_w$ and $100\nu_w$ being out of phase by 21° and 41°, respectively (cf. Figures 6b and 6c).

The different flow dynamics occurring for high and low viscous fluids were summarised in a flow transition map based on Fr and Re, where four main regions were identified to discriminate between the different in-phase and out-of-phase flows associated to different ν (cf. Figure 8). A non-dimensional reference velocity of the turbulent velocity fluctuations was defined to assess how the turbulence levels changed with varying Fr and Re. It was found that turbulence levels rise when a low viscous fluid is considered and the flow is out-of-phase (i.e. combination of high Fr and Re). The variation of the turbulent kinetic energy content was further investigated considering three different Re obtained with combinations of ν and d_i. The data show that turbulence growth is promoted or retarded depending on the transitional Fr_c set by the operating conditions (i.e. d_o, d_i, ν, N, h). Even data for the same Re displayed different behaviour, with turbulence content of more viscous fluids obtained in a larger cylinder rising at a lower transitional Fr_c than that obtained with water in a smaller one (cf. Figure 9a). To better compare the data sets obtained at different Re and overcome their differences in terms of transitional Fr_c, a turbulent kinetic energy scaling methodology based on the ratio Fr/Fr_c is proposed in Figure 9b. This normalisation proved to be effective as the curves associated to the different Re collapsed on each other, and can help to explain the nearly constant mixing number obtained by Rodriguez et al.[18] for $Fr/Fr_c \geq 1.4$.

A 2D analysis was carried out to investigate the strain and shear rates in the cylindrical bioreactor. A linear increase with Froude number was observed for the space averaged strain/shear rate considered, with the axial strain and shear rates, $|S_{zz}|^*$=$|S_{rz}|^*$=0-1.4πN, being greater than the radial strain rate, $|S_{rr}|^*$=0-1πN, over the Froude number range investigated. The distribution of the rate of viscous dissipation of kinetic energy in the bioreactor was determined by means of PIV measurements, and the associated power consumption was consumption found to be consistent with that determined by[13] for a similar system through torque measurements. The effect of spatial resolution on the estimation of the energy dissipation and of the Kolmogoroff length scale was investigated, and it was observed that for high spatial resolution ($\frac{\Delta x}{d_i}$=1.2×10^{-3}) the normalised ϵ for ϕ=270° was twice that for ϕ=0°. Furthermore, the normalised dissipation rate varied significantly with spatial resolution, as values of the dissipation rate at the highest spatial resolution, $\frac{\Delta x}{d_i}$=1.2×10^{-3}, were 10 times greater than those obtained at the lowest spatial resolution investigated ($\frac{\Delta x}{d_i}$=1.3×10^{-2}). This analysis indicates that both the measurement spatial resolution and the Froude number, Fr, have a great impact on the estimated size of the dissipative eddies, and careful selection of the spatial resolution, especially at high Fr, should be sought to produce reliable results that can advise on bioprocess design.

The current results provide a better understanding of the physics and turbulence transition occurring in orbitally shaken bioreactors and future work to elucidate further the mixing mechanisms in such systems is called for. Nevertheless, the results of the present work show promise for a more reliable and accurate characterization of OSB for improved bioprocess design methodologies, and research is on-going at present to assess the flow scaling identified in this work for fluid of varying viscosity when a two-phase system with commercial microcarriers suspended in the media is employed.

Acknowledgements

Financial support for the work reported here was provided by the Engineering and Physical Sciences Research Council (EPSRC) of the UK, grant EP/E055958. I want to thank Prof. Yianneskis for the useful discussions.

References

1. Liu, C., Hong, L.. Development of a shaking bioreactor system for animal cell cultures. *Biochem Eng J* 2001;7(2):121–125.

2. Zhang, X., Stettler, M., Sanctis, D.D., Perrone, M., Parolini, N., Discacciati, M., Jesus, M.D., Hacker, D., Quarteroni, A., Wurm, F.. Use of orbital shaken disposable bioreactors for mammalian cell cultures from the milliliter-scale to the 1000-liter scale. *Advan Biochem Eng Biotechnol* 2010;115:33–53.

3. Klöckner, W., Büchs, J.. Advances in shaking technologies. *Trends Biotechnol* 2012;30:307–314.

4. Büchs, J., Maier, U., Milbradt, C., Zoels, B.. Power consumption in shaking flasks on rotatory shaking machines: I. Power consumption measurement in unbaffled flasks at low liquid viscosity. *Biotechnol Bioeng* 2000;68:589–593.

5. Maier, U., Losen, M., Büchs, J.. Advances in understanding and modeling the gas-liquid mass transfer in shake flasks. *Biochemcial Eng J* 2004;17:155–167.

6. Micheletti, M., Barret, T., Doig, S., Baganz, F., Levy, M., Woodley, J., Lye, G.. Fluid mixing in shaken bioreactors: Implications for scale-up predictions from microlitre-scale microbial and mammalian cell cultures. *Chem Eng Scien* 2006;61:2939–2949.

7. Zhang, H., Lamping, S., Pickering, S., Lye, G., Shamlou, P.. Engineering characterisation of a single well from 24-well and 96-well microtitre plates. *Biochemical Eng J* 2008;40:138–149.

8. Peter, C., Lotter, S., Maier, U., Büchs, J.. Impact of out-of-phase conditions on screening results in shaking flask experiments. *Biochemical Eng J* 2004;17:205–215.

9. Büchs, J., Maier, U., Milbradt, C., Zoels, B.. Power consumption in shaking flasks on rotary shaking machines: II. Nondimensional description of specific power consumption and flow regimes in unbaffled flasks at elevated liquid viscosity. *Biotechnol Bioeng* 2000;68:594–601.

10. Kim, H., Kizito, P.. Stirring free surface flows due to horizontal circulatory oscillation of partially filled container. *Chem Eng Commun* 2009;11:1300–1321.

11. Gardner, J., Tatterson, G.. Characterization of mixing in shaker table containers. *Biotechnol Bioeng* 1992;39:794–797.

12. Weheliye, W., Yianneskis, M., Ducci, A.. On the fluid dynamics of shaken bioreactors - flow characterization and transition. *AIChE J* 2013;59:334–344.

13. Klöckner, W., Tissot, S., Wurm, F., Büchs, J.. Power input correlation to characterize the hydrodynamics of cylindrical orbitally shaken bioreactors. *Biochemical Eng J* 2012;65:63–69.

14. Zhang, H., Dalson, W., Moore, E., Shamlou, P.. Computational fluid dynamics (CFD) analysis of mixing and gas liquid mass transfer in shake flasks. *Biotechnol Applicat Biochemical* 2005;41:1–8.

15. Discacciati, M., Hacker, D., Quarteroni, A., Quinodoz, S., Tissot, S., Wurm, F.. Numerical simulation of orbitally shaken viscous fluids with free surface. *Int J Numer Meth Fluids* 2013;71:294–315.

16. Zhang, X., Bürki, C., Stettler, M., Sanctis, D., Perrone, M., Discacciati, M., Parolini, N., DeJesus, M., Hacker, D., Quarteroni, A., Wurm, F.. Efficient oxygen transfer by surface aeration in shaken cylindrical containers for mammalian cell cultivation at volumetric scales up to 1000 l. *Biochemical Eng J* 2009;45:41–47.

17. Tissot, S., Farhat, M., Hacker, D., Anderlei, T., Kühner, M.. Determination of a scale-up factor from mixing time studies in orbitally shaken bioreactors. *Biochemical Eng J* 2010;52:181–186.

18. Rodriguez, G., Anderlei, T., Micheletti, M., Yianneskis, M., Ducci, A.. On the measurement and scaling of mixing time in orbitally shaken bioreactors. *Biochemical Eng J* 2014;82:10–21.

19. Nienow, A., Scott, W., Hewitt, C., Thomas, C., Lewise, G., Amanul-lah, A., Kiss, R., Meieer, S.. Scale-down studies for assessing the different stressparameters on growth and product quality during animal cell culture. *Chem Eng Res Des* 2013;91(11):2265–2274.

20. Ma, N., Koelling, K., Chalmers, J.. Fabrication and use of a transient contractional flow device to quantify the sensitivity of mammalian and insect cells to hydrodynamic forces. *Biotechnol Bioeng* 2002;80:428–437.

21. Nienow, A.W.. Reactor engineering in large scale animal cell culture. *Cytotechnology* 2006;50:9–33.

22. Hu, W., Berdugo, C., Chalmers, J.. The potential of hydrodynamic damage to animal cells of industrial relevance: current understanding. *Cytotechnology* 2011;63:445–460.

23. Sargent, C., Berguig, G., Kinney, M., Hiatt, L., Carpenedo, R., Berson, R., McDevitt, T.. Hydrodynamic modulation of embryonic stem cell differentiation by rotary orbital suspension culture. *Biotechnol Bioeng* 2010;105:611–626.

24. King, J., Miller, W.. Bioreactor development for stem cell expansion andcontrolled differentiation. *Curr Opin Chem Biol* 2007;11:394–398.

25. Eliase, C., Desai, R., Patale, M., Joshi, J., Mashelkar, R.A.. Turbulent shear stress-effect of mammalian cell culture and measurement using Laser Doppler Anemometer. *Chem Eng Sci* 1995;**50**:2431–2440.

26. Baldi, S., Yianneskis, M.. On the direct measurement of turbulence energy dissipation in stirred vessels with PIV. *Ind Eng Chem Res* 2003;42:7006–7016.

27. Ducci, A., Yianneskis, M.. Direct determination of dissipation rate in stirred vessels with multi-channel LDA. *AIChE J* 2005;51:2133–2149.

28. Escudié, R., Liné, A.. Experimental analysis of hydrodynamics in a radially agitated tank. *AIChE J* 2003;49(3):585 – 603.

29. Sharp, K., Adrian, R.. PIV study of small-scale flow structure around a rushton turbine. *AIChE J* 2001;47:766–778.

30. Rodriguez, G., Weheliye, W., Anderlei, T., M.Micheletti, , M.Yianneskis, , Ducci, A.. Mixing time and kinetic energy measurements in a shaken cylindrical bioreactor. *Chem Eng Res Des* 2013;81:331–341.

31. Kamruzzaman, M., Djenidi, L., Antonia, R.. Behaviours of energy spectrum at low reynolds numbers in grid turbulence. *International journal of Mechanical, Aerospace, Industrial and Mechatronics Engineering* 2013;7(12):1385–1389.

Nomenclature

Abbreviation

2D	Two-Dimensional
OSB	Orbitally shaken bioreactor
PIV	Particle Image Velocimetry

Greek Symbols

ϵ	Viscous dissipation rate of kinetic energy, $\mathrm{m}^2/\mathrm{s}^3$
η_k	Smallest dissipative scale, m
ν	Kinematic viscosity, m^2/s
ν_w	Kinematic viscosity of water, m^2/s
ϕ	Phase angle of the table, °
ω_i	Vorticity components in the ith direction, s^{-1}
ω^*	Space average vorticity for phase resolved flow field, s^{-1}
$\overline{\omega}^*$	Space average vorticity for ensemble-average flow field, s^{-1}

Roman Symbols

a_o	Constant of proportionality, -
a_{ow}	Constant of proportionality for water, m
d_i	Inner diameter of the cylinder, m
d_o	Orbital diameter, m
Fr	Froude number, -
Fr_c	Critical/transitional Froude number, -
g	Gravitational acceleration, m/s^2
h	Fluid height at rest, m
h_f	Fluid height at the left hand side wall, m
Δh	Free surface height, m
N	Shaken rotational speed, s^{-1}
P_v	Volumetric power consumption, $\mathrm{kg}/(\mathrm{m\ s}^3)$
Re	Reynolds number, -
S_{ij}	Strain rate tensor, s^{-1}
S^*_{ij}	Space average of the strain rate tensor, s^{-1}
ΔT	Time between two consecutive images, s
T^*	Space average of the circulation time for the phase average flow field, s
$\overline{T}^*$	Space average of the circulation time for the ensemble-average flow field, s
u_i	Velocity in the ith direction, m/s
$\langle u_i \rangle$	Phase average of the velocity component in the ith direction, m/s
u'_i	Random velocity fluctuations in the ith direction, m/s

List of Figures

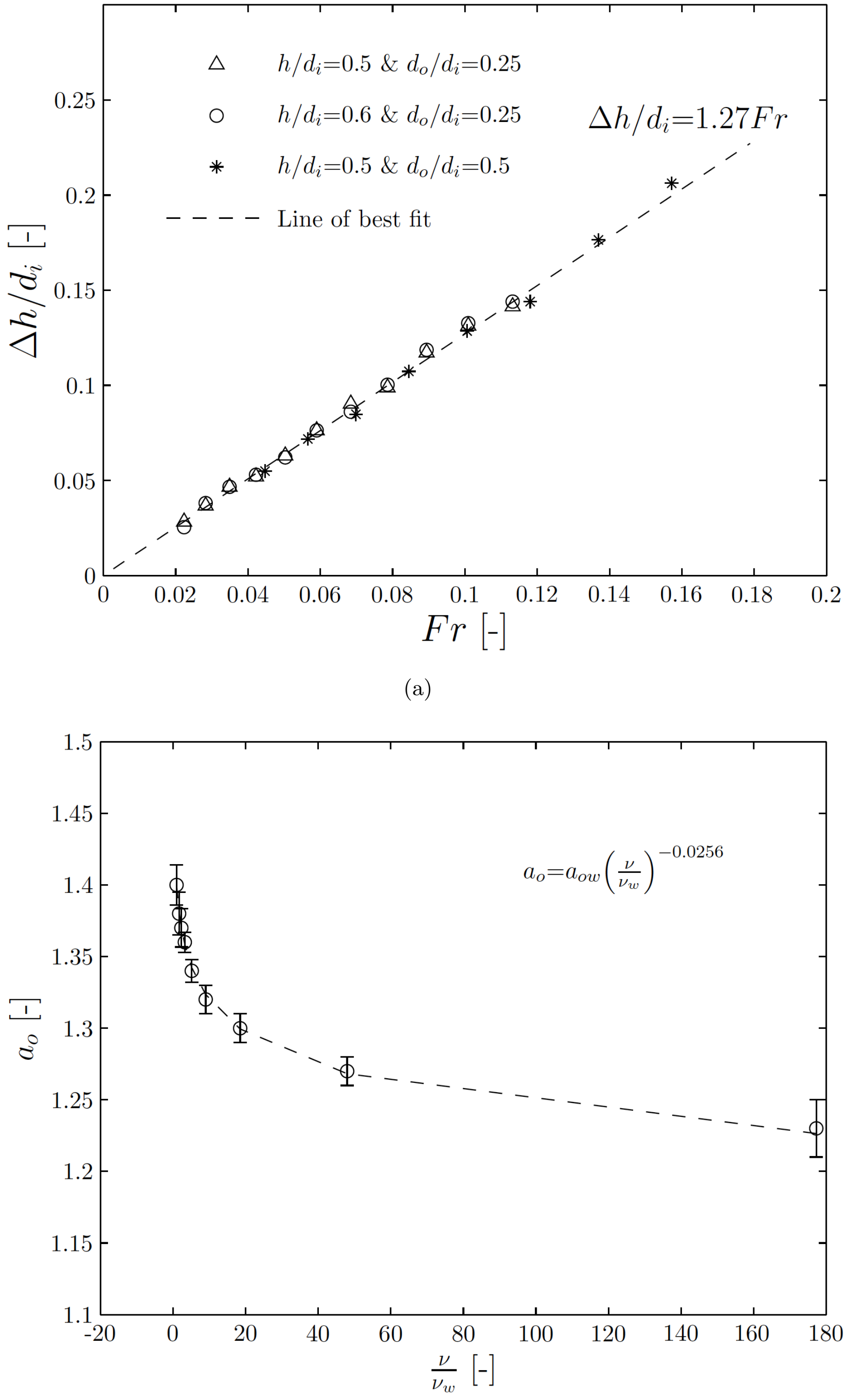

(a)

(b)

Figure 1: (a) Variation of the free surface inclination with Fr for ν=4.97×10^{-5} $\mathrm{m^2s^{-1}}$, (ϕ=0°); (b) Variation of the free surface constant of proportionality, a_o, for increasing fluid viscosity, ν.

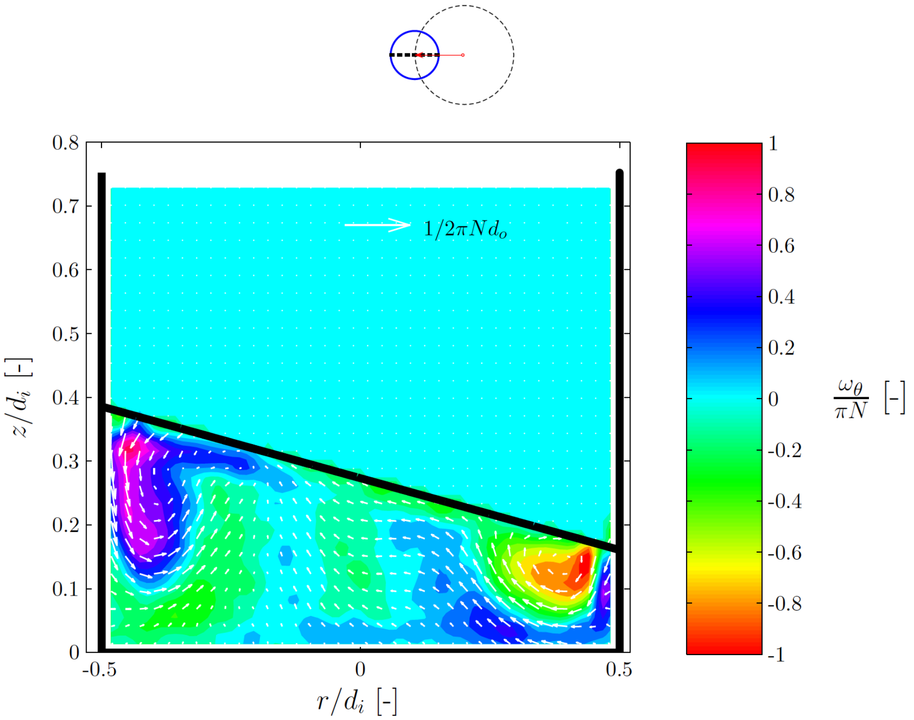

(a)

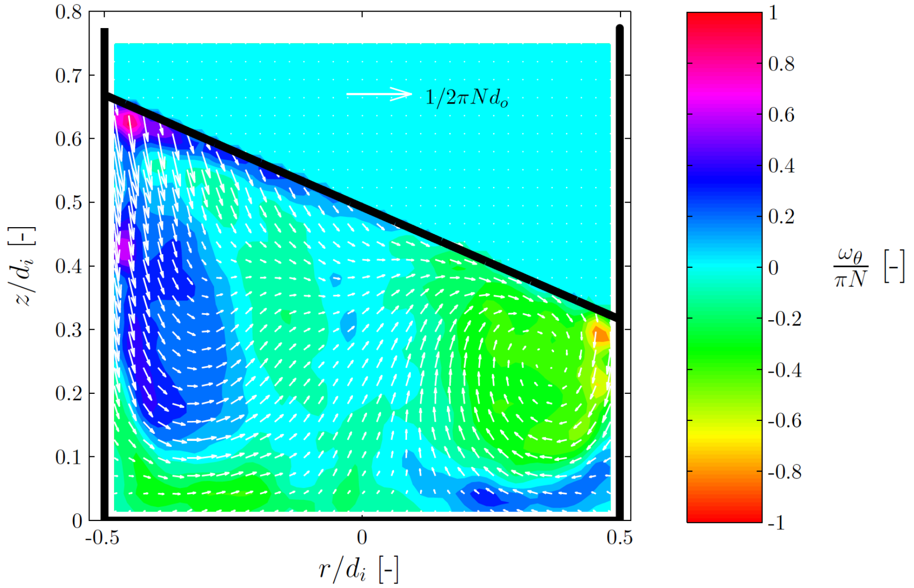

(b)

Figure 2: Phase-resolved vector fields and contour plots of the tangential component of the vorticity, ω_θ, for ν=1.7×10^{-6} m^{2}s^{-1} (ϕ=0°, d_o/d_i=0.5): (a) h/d_i=0.3 and Fr=0.16 (N=75 rpm); (b) h/d_i=0.5 and Fr=0.25 (N=95rpm).

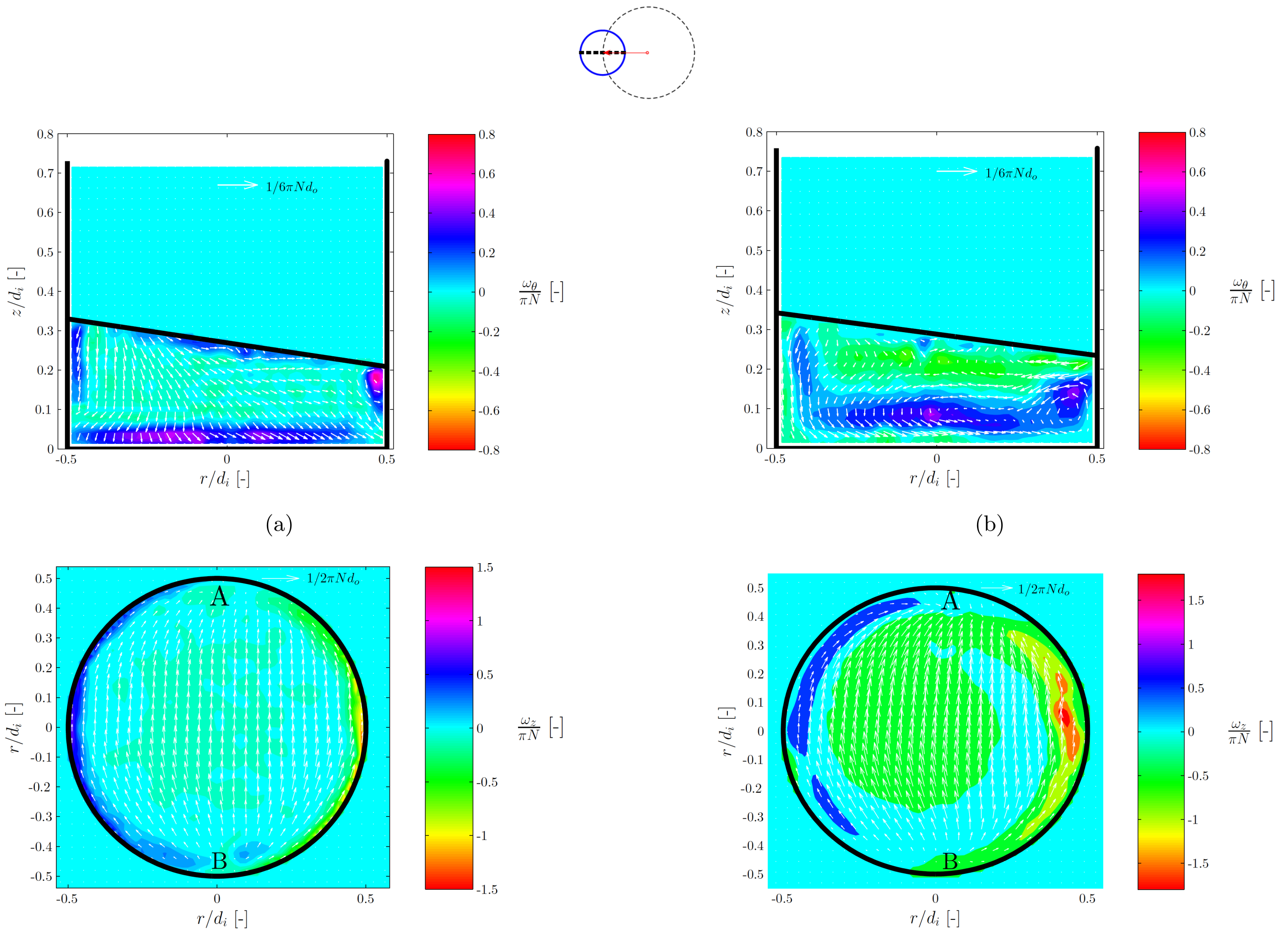

(a)

(b)

(c)

(d)

Figure 3: Phase-resolved vector fields and contour plots of the tangential and axial components of the vorticity, ω_θ and ω_z (h/d_i=0.3, ϕ=0°, d_o/d_i=0.25, Fr=0.09): (a) Vertical plane, ν=1×10^{-5} m^{2}s^{-1}; (b) Vertical plane, ν=1×10^{-4} m^{2}s^{-1}; (c) Horizontal plane, ν=1×10^{-5} m^{2}s^{-1} (z/d_i=0.1); (d) Horizontal plane, ν=1×10^{-4} m^{2}s^{-1} (z/d_i=0.1).

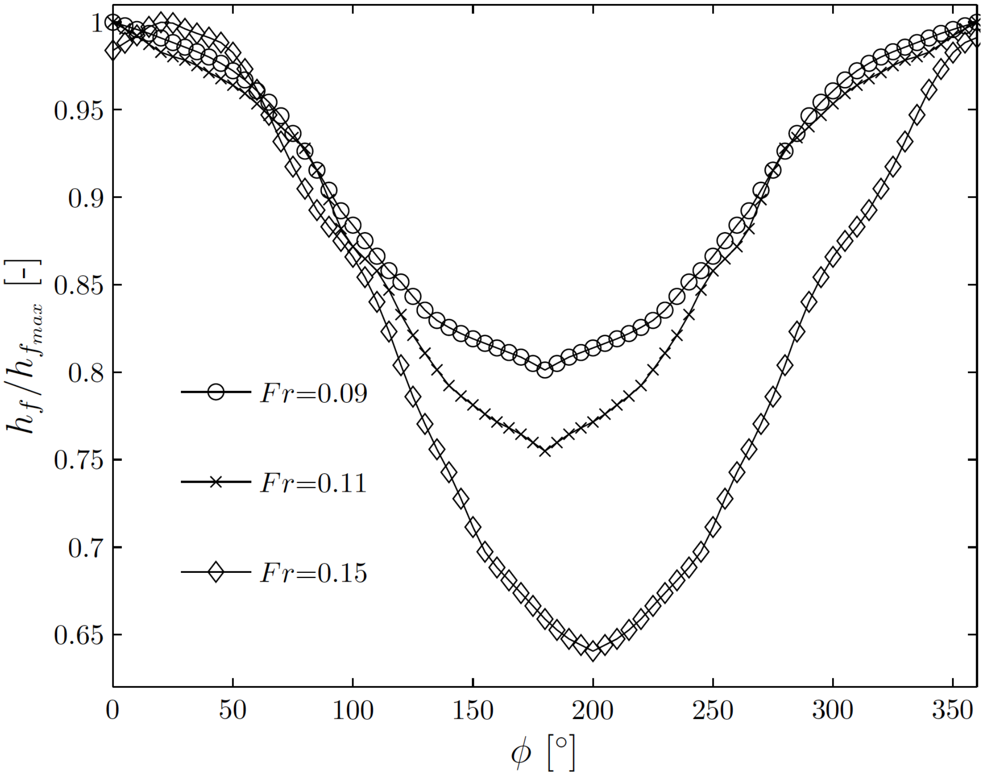

Figure 4: Variation of the non-dimensional free surface height at the left side wall, $h_f/h_{f_{max}}$, with phase angle, ϕ, for ν=1×10^{-5} m^{2}s^{-1} (h/d_i=0.3, d_o/d_i=0.25).

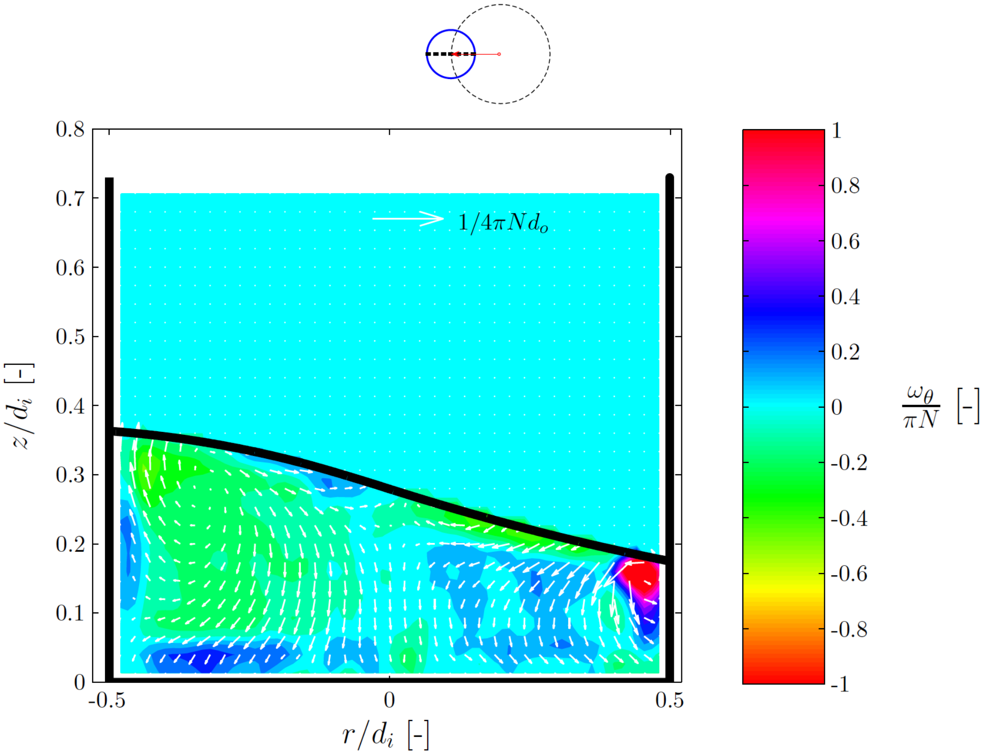

Figure 5: Phase-resolved vector fields and contour plots of the tangential component of the vorticity, ω_θ, for ν=1×10^{-5} m^{2}s^{-1} and Fr=0.14 (h/d_i=0.3, ϕ=0°, d_o/d_i=0.25).

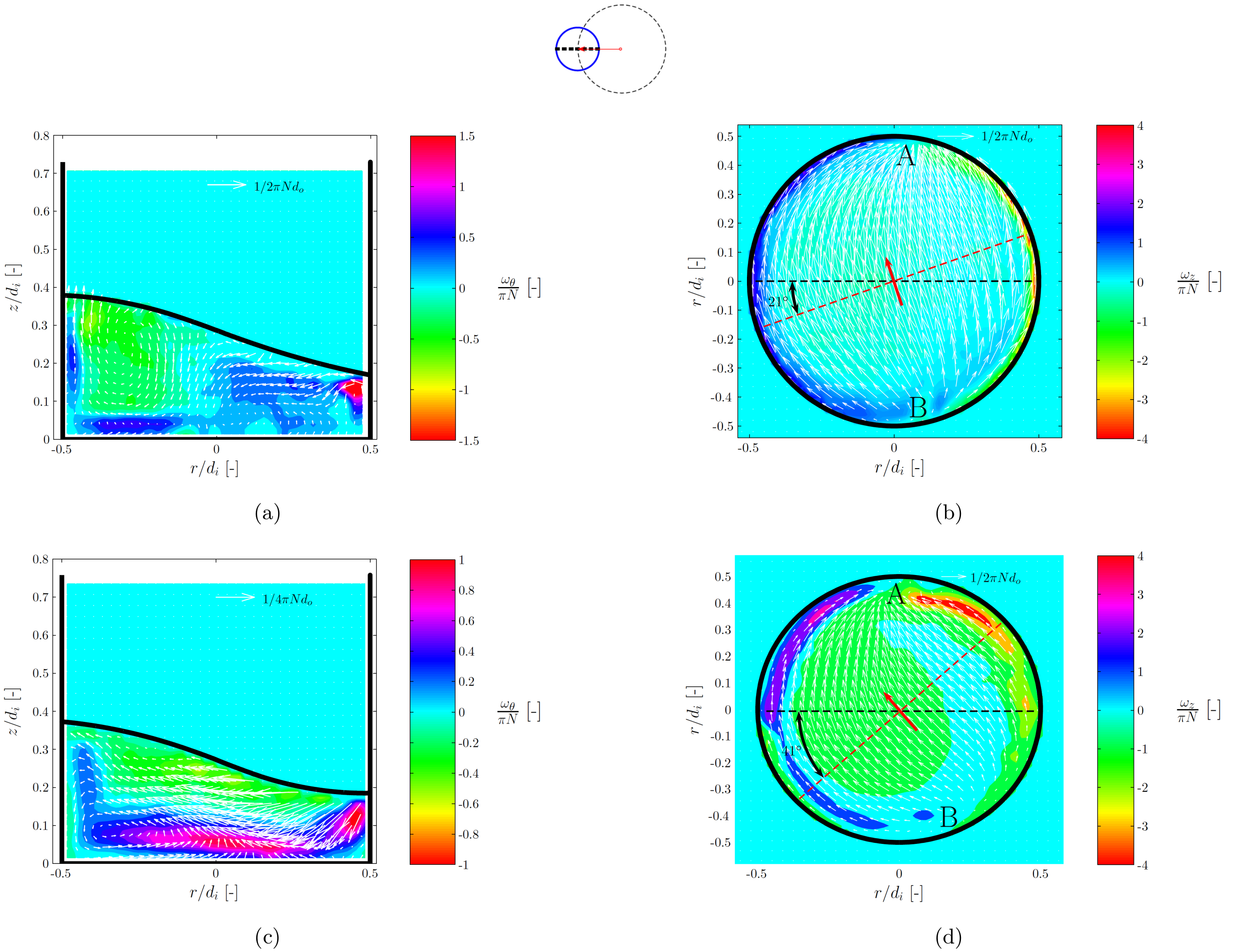

Figure 6: Phase-resolved vector fields and contour plots of the tangential and axial components of the vorticity, ω_θ and ω_z (h/d_i=0.3, ϕ=0°, d_o/d_i=0.25): (a) Vertical plane, ν=1×10^{-5} m^{2}s^{-1} and Fr=0.17 (N=110 rpm); (b) Horizontal plane, ν=1×10^{-5} m^{2}s^{-1} Fr=0.17 (z/d_i=0.1); (c) Vertical plane, ν=1×10^{-4} m^{2}s^{-1} and Fr=0.14 (N=100 rpm) (d) Horizontal plane, ν=1×10^{-4} m^{2}s^{-1} Fr=0.14 (z/d_i=0.1).

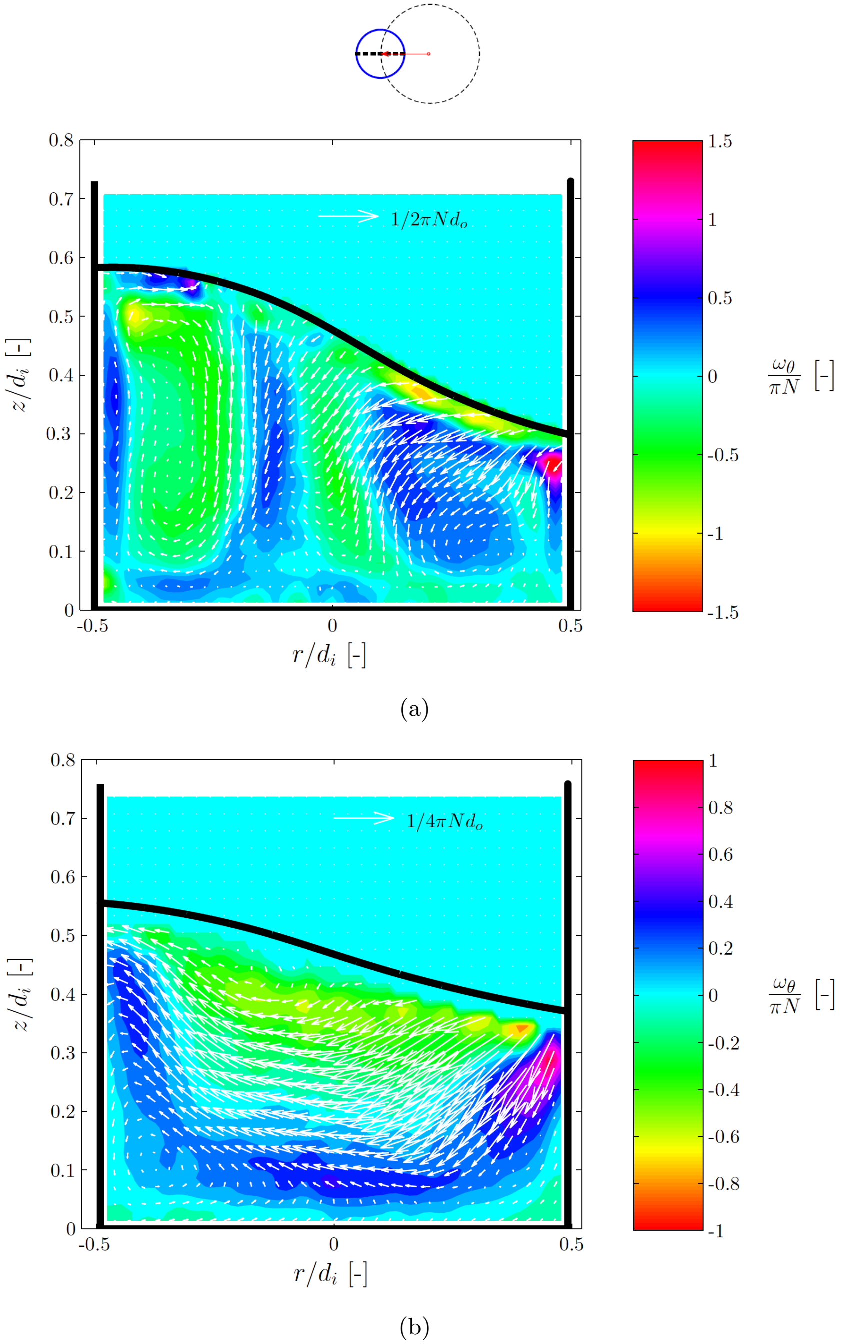

Figure 7: Phase-resolved vector fields and contour plots of the tangential component of the vorticity, ω_θ, for h/d_i=0.5 (ϕ=0°, d_o/d_i=0.25): (a) Fr=0.2 (N=120 rpm) and $\nu=1\times10^{-5}$ m^{2}s^{-1}; (b) Fr=0.15 (N=102 rpm) and $\nu=1\times10^{-4}$ m^{2}s^{-1}.

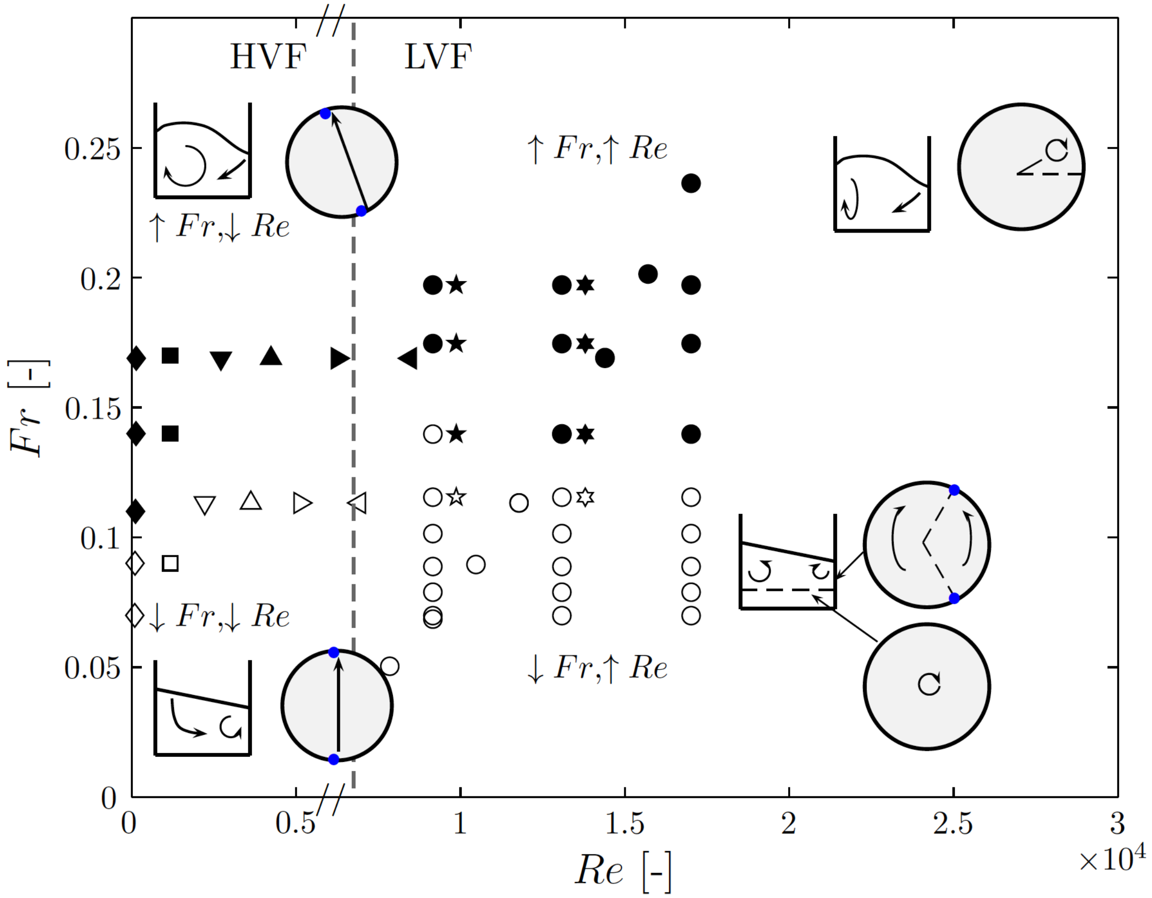

Figure 8: Map of the combinations of Fr and Re examined with schematic visualisations of the associated in-phase and out-of-phase flow fields (h/d_i=0.3).

Low Viscous Fluids (LVF): ν=1×10^{-6} m^{2}s^{-1} (○ in-phase, ● out-of-phase), ν=1.3×10^{-6} m^{2}s^{-1} (✡ in-phase, ✶ out-of-phase), ν=1.4×10^{-6} m^{2}s^{-1} (☆ in-phase, ★ out-of-phase), ν=1.7×10^{-6} m^{2}s^{-1} (◁ in-phase, ◀ out-of-phase);

High Viscous Fluids (HVF): ν=2.3×10^{-6} m^{2}s^{-1} (▷ in-phase, ▶ out-of-phase), ν=3.25×10^{-6} m^{2}s^{-1} (△ in-phase, ▲ out-of-phase), ν=5.3×10^{-6} m^{2}s^{-1} (▽ in-phase, ▼ out-of-phase), ν=1×10^{-5} m^{2}s^{-1} (□ in-phase, ■ out-of-phase), ν=1×10^{-4} m^{2}s^{-1} (◊ in-phase, ♦ out-of-phase).

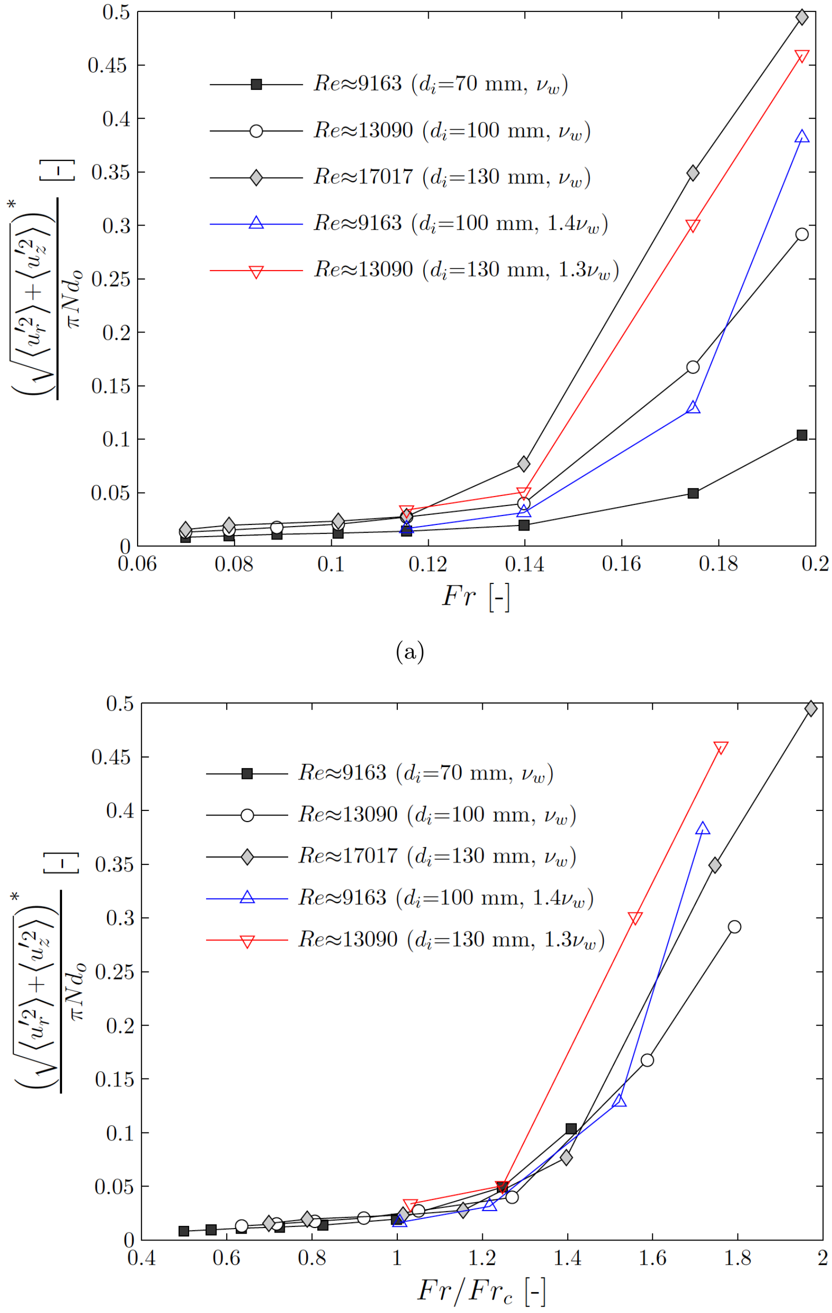

(a)

(b)

Figure 9: Variation of the turbulent kinetic energy reference velocity with Froude number, Fr, (a) and Fr/Fr_c (b) for three sets of Reynolds number.

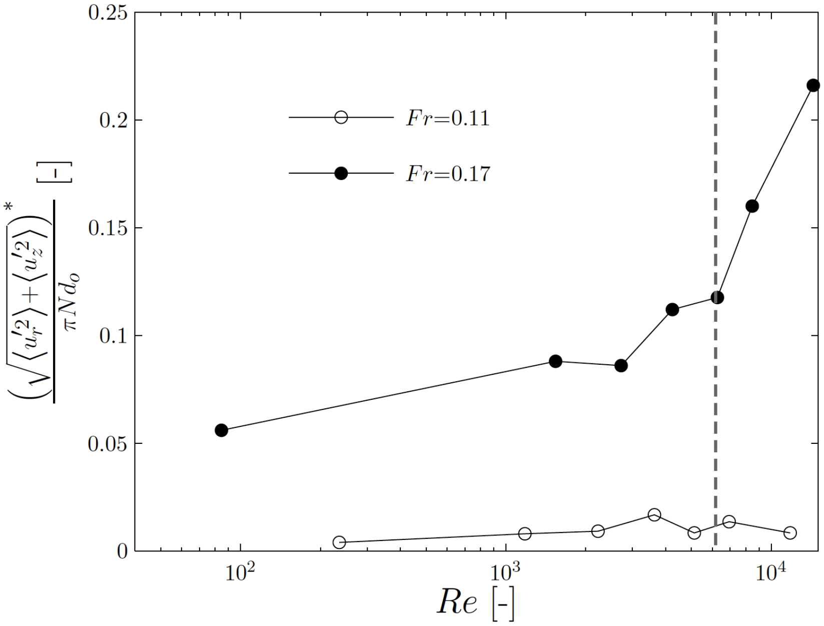

Figure 10: Variation of the turbulent kinetic energy reference velocity, $\left(\sqrt{\langle u_r'^2\rangle + \langle u_z'^2\rangle}\right)^*$, with Re for high and low Fr.

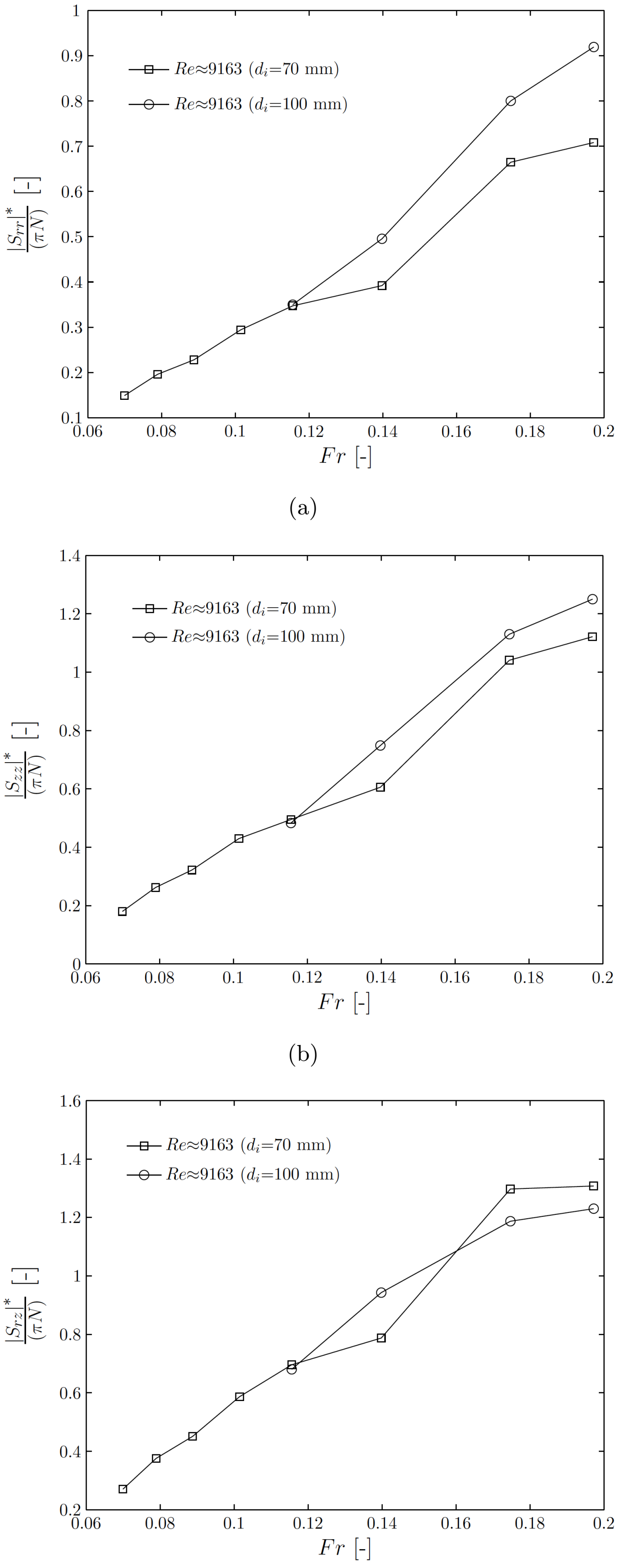

(a)

(b)

(c)

Figure 11: Variation of the space-averaged strain and shear rates with increasing Fr (h/d_i=0.3, ϕ= 270°); (a) $|S_{rr}|^*$; (b) $|S_{zz}|^*$; (c) $|S_{rz}|^*$.

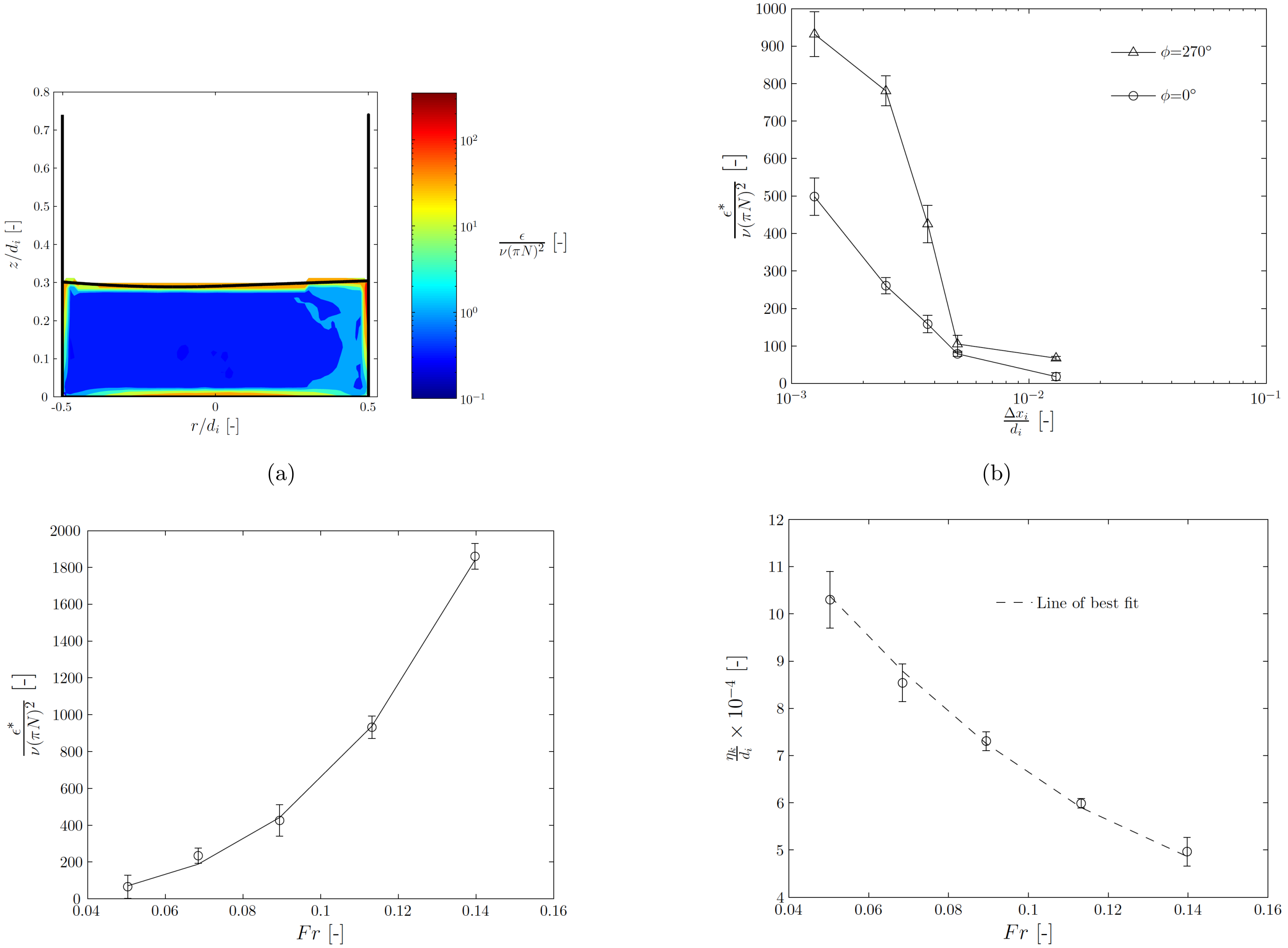

(a) (b)

(c) (d)

Figure 12: (a) Contour plot of the viscous dissipation rate of kinetic energy, ϵ (ϕ=270°, Fr=0.11, h/d_i=0.3, and d_o/d_i=0.25); (b) Variation of ϵ^* with decreasing spatial resolution, Δx_i, (h/d_i=0.3, d_o/d_i=0.25 and Fr=0.11); (c) Variation of ϵ^* with increasing Fr; (d) Variation of η_k with Fr (h/d_i=0.3, ϕ=270°, d_o/d_i=0.25).

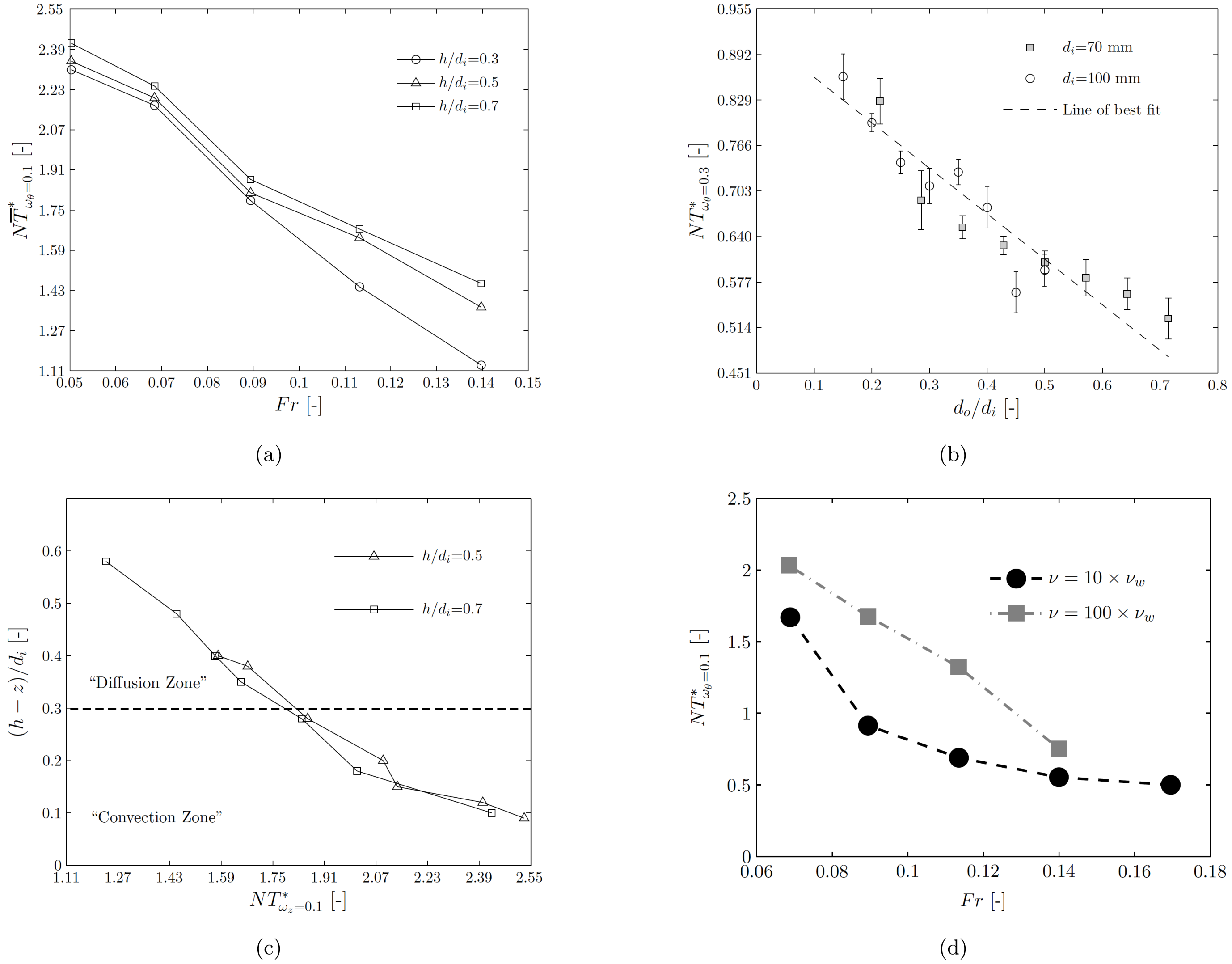

(a)

(b)

(c)

(d)

Figure 13: (a) Variation of the ensemble-averaged non-dimensional circulation time, $N\overline{T}^*_{\omega\theta=0.1}$, with increasing Fr for h/d_i=0.3, 0.5 and 0.7; (b) Variation of the non-dimensional circulation time, $NT^*_{\omega\theta=0.3}$, of the right vortex with increasing d_o/d_i for a flow condition incipient out-of-phase transition (h/d_i=0.3 and ϕ=0°); (c) Variation of the space-averaged non-dimensional circulation time, $NT^*_{\omega z=0.1}$, against the axial coordinate, $(h-z)/d_i$ for Fr=0.11 (N=90 rpm); (d) Variation of the phase-resolved non-dimensional circulation time, $NT^*_{\omega\theta=0.1}$, with increasing Fr for fluids of high viscosity.